

# Linked 3-D modelling of megathrust earthquake-tsunami events: from subduction to tsunami run up

E.H. Madden<sup>1,2</sup>, M. Bader,<sup>3</sup> J. Behrens,<sup>4</sup> Y. van Dinther<sup>5,6</sup>, A.-A. Gabriel<sup>1</sup>, L. Rannabauer,<sup>3</sup> T. Ulrich,<sup>1</sup> C. Uphoff,<sup>1,3</sup> S. Vater<sup>4,\*</sup> and I. van Zelst<sup>5,†</sup>

<sup>1</sup>Department of Earth and Environmental Sciences, Ludwig-Maximilians-Universität München, Munich, Germany. E-mail: [betsymadden@gmail.com](mailto:betsymadden@gmail.com)

<sup>2</sup>Observatório Sismológico, Instituto de Geociências, Universidade de Brasília, Brasília, Brazil

<sup>3</sup>Department of Informatics, Technical University of Munich, Garching, Germany

<sup>4</sup>Department of Mathematics/CEN, Numerical Methods in Geosciences, Universität Hamburg, Hamburg, Germany

<sup>5</sup>Department of Earth Sciences, Seismology and Wave Physics, Institute of Geophysics, ETH Zürich, Zürich, Switzerland

<sup>6</sup>Department of Earth Sciences, Utrecht University, Utrecht, The Netherlands

Accepted 2020 October 8. Received 2020 September 7; in original form 2020 September 7

## SUMMARY

How does megathrust earthquake rupture govern tsunami behaviour? Recent modelling advances permit evaluation of the influence of 3-D earthquake dynamics on tsunami genesis, propagation, and coastal inundation. Here, we present and explore a virtual laboratory in which the tsunami source arises from 3-D coseismic seafloor displacements generated by a dynamic earthquake rupture model. This is achieved by linking open-source earthquake and tsunami computational models that follow discontinuous Galerkin schemes and are facilitated by highly optimized parallel algorithms and software. We present three scenarios demonstrating the flexibility and capabilities of linked modelling. In the first two scenarios, we use a dynamic earthquake source including time-dependent spontaneous failure along a 3-D planar fault surrounded by homogeneous rock and depth-dependent, near-lithostatic stresses. We investigate how slip to the trench influences tsunami behaviour by simulating one blind and one surface-breaching rupture. The blind rupture scenario exhibits distinct earthquake characteristics (lower slip, shorter rupture duration, lower stress drop, lower rupture speed), but the tsunami is similar to that from the surface-breaching rupture in run-up and length of impacted coastline. The higher tsunami-generating efficiency of the blind rupture may explain how there are differences in earthquake characteristics between the scenarios, but similarities in tsunami inundation patterns. However, the lower seafloor displacements in the blind rupture result in a smaller displaced volume of water leading to a narrower inundation corridor inland from the coast and a 15 per cent smaller inundation area overall. In the third scenario, the 3-D earthquake model is initialized using a seismo-thermo-mechanical geodynamic model simulating both subduction dynamics and seismic cycles. This ensures that the curved fault geometry, heterogeneous stresses and strength and material structure are consistent with each other and with millions of years of modelled deformation in the subduction channel. These conditions lead to a realistic rupture in terms of velocity and stress drop that is blind, but efficiently generates a tsunami. In all scenarios, comparison with the tsunamis sourced by the time-dependent seafloor displacements, using only the time-independent displacements alters tsunami temporal behaviour, resulting in later tsunami arrival at the coast, but faster coastal inundation. In the scenarios with the surface-breaching and subduction-initialized earthquakes, using the time-independent displacements also overpredicts run-up. In the future, the here presented scenarios may be useful for comparison of alternative dynamic earthquake-tsunami modelling approaches or linking choices, and can be readily developed into more complex

\* Now at: Department of Mathematics and Computer Science, Freie Universität Berlin, Berlin, Germany

† Now at: Institute of Geophysics and Tectonics, School of Earth and Environment, University of Leeds, Leeds, LS29JT, United Kingdom

applications to study how earthquake source dynamics influence tsunami genesis, propagation and inundation.

**Key words:** Tsunamis; Seismic cycle; Numerical modelling; Earthquake dynamics; Earthquake hazards; Subduction zone processes.

## 1 INTRODUCTION

Subduction zone earthquakes can trigger devastating tsunamis, such as the 2004 Sumatra, 2010 Maule and 2011 Tohoku earthquake-tsunami sequences. Numerical models of tsunami generation, propagation and inundation use observations and data inversions to both characterize the tsunami source and constrain simulation results. However, in many instances, the observed tsunami behaviour is unexpected or tsunamis occur from unexpected sources (e.g. Jamelot *et al.* 2019; Ulrich *et al.* 2019b). Recent, well-recorded events highlight the importance of dynamic tsunami source complexity. Tsunami generation may be impacted by splay faulting (Wendt *et al.* 2009; Geist & Oglesby 2014; Kozdon & Dunham 2014), long source duration (Maeda & Furumura 2011), horizontal momentum transfer (Song *et al.* 2008; Lotto *et al.* 2017b; Amlani *et al.* 2019) and mixed faulting mechanisms (e.g. Saito 2017; Ulrich *et al.* 2019b). These characteristics can be captured in dynamic earthquake rupture models, which aim to reproduce the physical processes that govern the way fault systems yield and slide (e.g. Andrews 1976; Oglesby *et al.* 2000; Day *et al.* 2005; Kaneko *et al.* 2008).

Computational advances now allow earthquake modelling to capture rupture dynamics on complex faults or fault systems on the scale of megathrust events (e.g. Murphy *et al.* 2016; Uphoff *et al.* 2017; Murphy *et al.* 2018; Ramos & Huang 2019). In addition, such models can include physical processes non-linearly coupled to the earthquake dynamics, such as off-fault plasticity (e.g., Andrews 2005; Dunham *et al.* 2011; Gabriel *et al.* 2013; Roten *et al.* 2014; Wollherr *et al.* 2018) or thermal pressurization of pore fluids (e.g., Bizzarri & Cocco 2006; Noda 2008; Gabriel *et al.* 2020). Such methods have realized realistic, observationally constrained simulations of several recent earthquakes, including the highly segmented crustal 2019 Ridgecrest, 2016 Kaikoura, 2010 Haiti, and 1992 Landers ruptures (Douilly *et al.* 2015; Ando & Kaneko 2018; Klinger *et al.* 2018; Ulrich *et al.* 2019a; Wollherr *et al.* 2019; Lozos & Harris 2020), the supershear 2018 Palu, Sulawesi earthquake (Amlani *et al.* 2019; Ulrich *et al.* 2019b), the 2015 Gorkha earthquake (Weng & Yang 2018; Wang *et al.* 2019), and large megathrust events (Galvez *et al.* 2014; Ma & Nie 2019; Ulrich *et al.* 2020). These models show that dynamic earthquake rupture models are ready to provide mechanically viable tsunami source descriptions. However, incorporating these into tsunami modelling is not trivial.

Tsunami modelling is undertaken with varying degrees of complexity. The application of normal mode theory was an early development (e.g. Ward 1980; Okal 1982) and has been adapted to include propagation of dispersive waves (Watada *et al.* 2014). Several hydrological tsunami models use a set of 2-D simplifications of the non-linear Navier–Stokes equations, such as the shallow water equations (e.g. Berger *et al.* 2011; Heidarzadeh *et al.* 2017) or Boussinesq type equations to model dispersive waves (e.g. Shi *et al.* 2012). These tsunami models use more or less sophisticated approximations to the earthquake induced uplift as initial conditions (for a review see e.g. Behrens & Dias 2015).

To set tsunami model initial conditions, earthquake-induced seafloor displacements often are determined using an analytical

solution for displacement due to a uniform rectangular dislocation within a homogeneous elastic half space (e.g. Okada 1985). A dislocation model may be taken from a finite fault model constrained by data inversion (e.g. Ji *et al.* 2002; Mai & Thingbaijam 2014; Bletery *et al.* 2016) as done by Allgeyer & Cummins (2014) and Jamelot *et al.* (2019), or designed to test certain source parameters as done by Geist & Yoshioka (1996). Stochastic models of seismogenic tsunami generation (e.g. Davies 2019) can either specify static slip on the fault following Andrews (1980) together with the idea that the final slip distribution after an earthquake rupture is self-affine, or use earthquake rupture models in the presence of stochastic stress (Geist & Oglesby 2014). In the context of an early warning system in Indonesia, complexity in space and time is achieved by including a grid of slip patches that together comprise a complex source model (Babeyko *et al.* 2010). Goda *et al.* (2014) highlight strong sensitivity of tsunami wave heights to site location and slip characteristics, and also to variations in dip, in stochastic random-field slip models for the 2011 Tohoku earthquake.

Several approaches also incorporate seismic waves into tsunami models. Saito *et al.* (2019) present a 2-step tsunami modelling method: first, the spatial and temporal evolution of seafloor surface height is determined from a seismic wave simulation; second, this vertical velocity is used to source a 2-D, non-linear hydrodynamic tsunami model. As an earthquake source, Saito *et al.* (2019) use a series of dislocations derived from dynamic rupture modelling of a potential future earthquake rupture in the Nankai Trough, Japan by Hok *et al.* (2011). Maeda *et al.* (2013) perform tsunami models of the 2011 Tohoku earthquake using tsunami-coupled equations of motion solved by the finite difference method (Maeda & Furumura 2011); these incorporate seismic waves and seafloor displacements generated from a 3-D kinematic earthquake source.

Use of a data-driven finite earthquake source model to determine seafloor initial conditions for the tsunami model is advantageous when trying to understand a specific event. However, earthquake source imaging can suffer from inherent non-uniqueness (e.g. Mai *et al.* 2016). Moreover, in a tsunami hazard context, observations are not readily available to constrain future earthquake sources, motivating stochastic approaches for example (e.g. McCloskey *et al.* 2008). While alternative approaches avoid characterization of fault slip altogether by using data assimilation (e.g. Maeda *et al.* 2015) or a double-couple source (e.g. Maeda *et al.* 2011), another way forward is incorporating earthquake rupture dynamics directly into tsunami models as the tsunami source. Ryan *et al.* (2015) use the final (time-independent) displacements from 3-D dynamic rupture models of earthquakes on faults in offshore California as the tsunami source in models using the nonlinear shallow water equations solved by a finite difference scheme. Wendt *et al.* (2009) use the 3-D, time-dependent displacements from dynamic rupture on a 3-D fault with two planar segments (megathrust and splay) as the source for shallow-water, hydrodynamic tsunami models solved with finite difference methods. Dynamic modelling also may be used to produce stochastic models of tsunami generation and propagation as shown by Geist & Oglesby (2014), who use a stochastic distribution of shear stress on the fault system and run multiple realizations of the random variables to produce a suite of earthquake and tsunami

models. Time-dependent, 3-D displacements from large-scale rupture scenarios of the 2018 Sulawesi earthquake and 2004 Sumatra earthquake, incorporating complex fault geometry and constitutive behaviour, are linked to a hydrostatic shallow water tsunami model by Ulrich *et al.* (2019b) and Ulrich *et al.* (2020). 2-D dynamic rupture simulations are fully coupled to the time-dependent response of water layers hosting tsunamis by Lotto *et al.* (2017a, b, 2018). As Lotto *et al.* (2017a) concludes, the deep insight gained from this narrow study of three earthquake initial conditions on earthquake and tsunami behaviour in 2-D underscores the need for more investigation into the influence of complex earthquake dynamics on tsunamis.

Here, we present methods to harness the potential of complex, 3-D dynamic rupture models as tsunami sources to enable direct studies of how earthquake initial conditions and earthquake dynamics affect tsunami genesis, propagation and inundation. These methods are based on the one-way linkage of a 3-D dynamic earthquake rupture and seismic wave propagation model with a hydrostatic shallow water tsunami model. Both computational models are open-source and based on the discontinuous Galerkin method. They are linked using the integrated vertical surface velocity from the earthquake model to yield time- and space-dependent displacements to source the tsunami model, similar to methods by Saito *et al.* (2019) and Ulrich *et al.* (2019b). The influence of the horizontal displacements are accounted for following Tanioka & Satake (1996). Because the displacements include fast waves that are not represented in the physical approximation of the hydrostatic model, we filter them by a spatial-temporal Fourier-transform.

We present two applications of this approach to earthquake-tsunami modelling, one simple and one more complex. The simple example links a rupture propagating across a gently dipping, planar fault surrounded by homogeneous, purely elastic media and an isotropic stress field. It includes two scenarios: one with high strength on the shallow fault leading to a blind rupture, and one with low strength on the shallow fault leading to a surface-breaching rupture. The seafloor displacements are Fourier-transform filtered in space and time to eliminate seismic waves that are incompatible with the hydrostatic, shallow water tsunami model. We compare both the earthquakes and the tsunamis in these two scenarios.

The second application uses a 2-D seismo-thermo-mechanical model simulating long term subduction dynamics and seismic cycles to initialize the 3-D dynamic earthquake rupture model (Fig. 1). Such TECSEAS models, bridging the time scales of tectonic (TEC) and seismic cycle (SEAS, Erickson *et al.* 2020) models, provide insight into the role of rheology, temperature, subduction dynamics, fault geometry, loading and evolution, including spontaneously evolving splay faults (e.g. van Dinther *et al.* 2013b, 2014; Sobolev & Muldashov 2017; Tong & Lavier 2018; Dal Zilio *et al.* 2019; D'Acquisto *et al.* 2020; Brizzi *et al.* 2020; Preuss *et al.* 2020). Earthquake rupture dynamics (including nucleation, propagation and arrest) are controlled by fault stress, strength and geometry and the surrounding material properties (e.g. Kame *et al.* 2003; Gabriel *et al.* 2012, 2013; Galis *et al.* 2015; Bai & Ampuero 2017; van Zelst *et al.* 2019). Although these initial conditions may be informed by laboratory and regional observations (e.g. Aochi & Fukuyama 2002; Agaard *et al.* 2004; Murphy *et al.* 2018; Ulrich *et al.* 2020), they remain difficult to constrain. This is particularly challenging in complex fault systems with lithological and geometric heterogeneities (e.g. Wendt *et al.* 2009), which impedes megathrust hazard assessment and mitigation. Constraints are particularly lacking in locations where observational data is sparse, either because earthquakes have not yet occurred or instrumentation is poor. Setting

the earthquake model initial conditions from a subduction model provides much needed constraint on the earthquake model initial conditions.

This approach also ensures self-consistency amongst initial conditions. For example, the assigned fault stress and strength are consistent with the fault geometry and material properties on and surrounding the fault. It also ensures self-consistency between those conditions and long-term subduction. For example, the assigned fault stress, strength and geometry are consistent with crustal, lithospheric and mantle deformation over geological timescales. In contrast to highly simplified earthquake models, subduction-initialized 2-D dynamic rupture models produce earthquakes with multiple rupture styles, shallow slip accumulation and fault reactivation (van Zelst *et al.* 2019).

Here, we extend the approach that initializes a 2-D dynamic earthquake rupture with a subduction and seismic cycle model (van Zelst *et al.* 2019) to a 3-D dynamic earthquake rupture. The linked initial conditions include a curved, blind fault geometry, heterogeneous fault stresses and strength, and spatially variable material properties. This linkage requires consideration of the incompressibility and viscoelasto-plastic, plane-strain conditions of the subduction model versus the compressible, elastic conditions of the earthquake model. The resulting 3-D dynamic rupture is linked with the tsunami model through the time-dependent seafloor displacements, following the same methods as in the first two examples.

For each application, we outline the methods, describe the resulting earthquake and tsunami, calculate the efficiency of each earthquake in generating that tsunami, and compare the tsunami results with those generated by a source incorporating the time-independent seafloor displacements from the end of the earthquake model. We emphasize that these applications demonstrate the capabilities of the modelling framework; future, more involved and complex applications will certainly result in further knowledge gain.

## 2 METHODS

The earthquake and tsunami computational models utilized here are open-source, use discontinuous Galerkin schemes, and are facilitated by highly optimized parallel algorithms and software. The methods for one-way linking between these models and for setting earthquake model initial conditions from a subduction geodynamic and seismic cycling code are outlined in the following.

As a note on terminology; we use ‘computational models’ to describe the computer programs discretizing the model equations and implementing the numerical workflow, and ‘physical models’ to describe the structural setups, governing equations and selected input parameters. A ‘scenario’ refers to the results achieved by a computational model according to a specific physical model. We attempt to only use ‘model’ when the use of the term is unambiguous.

### 2.1 Earthquake modelling with SeisSol

SeisSol is the computational model used to simulate 3-D dynamic earthquake rupture and seismic wave propagation (see Appendix A1). It solves the seismic wave equation in velocity-stress formulation using a Discontinuous Galerkin (DG) scheme with Arbitrary high-order DERivative (ADER) time stepping: ADER-DG (Dumbser & Käser 2006; Käser & Dumbser 2006). ADER is an explicit time-stepping method that achieves the same approximation order in space and time, but without requiring multiple stages for high discretization order, as in, for example Runge–Kutta

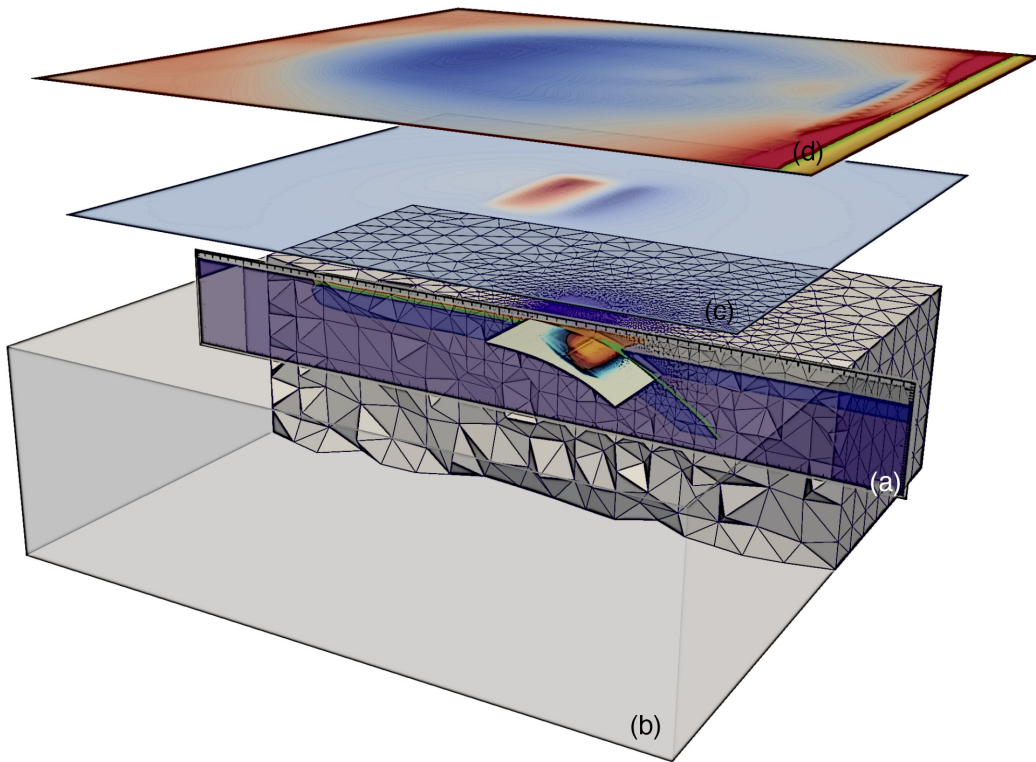


**Figure 1.** Illustration of model components of the presented virtual laboratory for earthquake-tsunami modelling. (a) 2-D subduction seismic cycling model used to initialize the 3-D earthquake model (Scenario C only), (b) 3-D dynamic earthquake rupture model, (c) seafloor displacement from the earthquake model used as the tsunami source in the tsunami model, (d) 2-D tsunami model. Note that dimensions are not to scale in all components.

schemes. The computational domain is discretized on a tetrahedral mesh, which simplifies automatic mesh generation for complicated geometries and facilitates static mesh adaptivity. Fast time to solution within SeisSol is enabled by recent hardware-aware computational optimizations targeting supercomputers with many-core CPUs (Breuer *et al.* 2014; Heinecke *et al.* 2014; Rettenberger *et al.* 2016) and an efficient local time-stepping algorithm (Breuer *et al.* 2016; Uphoff *et al.* 2017; Wolf *et al.* 2020). SeisSol has been validated against several community benchmarks (De La Puente *et al.* 2009; Pelties *et al.* 2012, 2014; Wollherr *et al.* 2018; Gabriel *et al.* 2020) following the SCEC/USGS Dynamic Rupture Code Verification exercises (Harris *et al.* 2009, 2018).

SeisSol is specifically suited to solve for rupture propagation along complex, 3-D fault geometries. Its scalability enables large and long dynamic rupture models. For example, scenarios of the 2004 Sumatra–Andaman earthquake with up to 220 million element meshes and order 6 accuracy in space and time ran in 13.9 hr on the SuperMUC phase2 supercomputer (86 016 cores) at the Leibniz Supercomputing Centre in Garching, Germany (Uphoff *et al.* 2017). Recent lower resolution scenarios require 4 hr on 5000 Sandy Bridge cores of the supercomputer SuperMucNG (Ulrich *et al.* 2020).

## 2.2 Tsunami modelling with sam(oa)<sup>2</sup>-flash

sam(oa)<sup>2</sup>-flash is the computational model used to simulate tsunami propagation and inundation (see Appendix A2). It solves the depth-integrated (hydrostatic) non-linear shallow water equations (e.g. LeVeque *et al.* 2011) using adaptive mesh refinement. It implements a second-order Runge–Kutta discontinuous Galerkin method on triangular grids (Cockburn & Shu 1998; Giraldo & Warburton 2008),

allowing wave propagation with high accuracy. sam(oa)<sup>2</sup>-flash features an accurate and robust wetting and drying scheme for the simulation of flooding and drying events at the coast (Vater & Behrens 2014; Vater *et al.* 2015, 2019). The scheme is mass-conservative, preserves positivity of the fluid depth and accurately computes small perturbations from the water state at rest (e.g. tsunami waves). Bottom friction is parametrized through Manning friction by a split-implicit discretization (Liang & Marche 2009). sam(oa)<sup>2</sup>-flash has been validated against a suite of benchmarks (Synolakis *et al.* 2008, see Appendix A2).

sam(oa)<sup>2</sup>-flash provides parallelization in shared (using OpenMP) and distributed (via MPI) memory (Meister *et al.* 2016). It scales up to thousands of compute cores, with problem sizes that exceed one billion grid cells with dynamic adaptive refinement and coarsening of cells (Meister *et al.* 2016). Efficient adaptive mesh refinement is based on tree-structured triangular meshes (see Appendix A2).

## 2.3 Linking methods and initial conditions

Fig. 1 shows schematically linkage between a subduction, earthquake and tsunami model. As we discuss here, this linkage requires consideration of assumptions inherent to each computational model, model dimensionality and the time and space scales efficiently spanned by the computational models.

### 2.3.1 Tsunami initial conditions

Linkage from an earthquake model to a tsunami model requires several considerations. The recorded extent and the sampling rate

of the domain and time frame of the earthquake model must be high enough to represent the required wavelength and frequency bands. For the transfer between models, the unstructured output from the earthquake model is bilinearly interpolated to an intermediate uniform Cartesian mesh. Also, we find that the earthquake model domain must be at least one fault length in each direction from the fault in order to minimize boundary effects. In terms of temporal resolution, we find that a 1 Hz sampling rate of the earthquake displacement field is sufficient, as it is much smaller than the typical temporal scale of a tsunami waves.

To build the tsunami source, the time-dependent variations in the 3-D vertical and horizontal coseismic seafloor displacements are mapped into vertical perturbations of the 2-D initial bathymetry field of the tsunami model, similar to the approaches in Saito *et al.* (2019), Wendt *et al.* (2009) and Ulrich *et al.* (2019b). The time-dependent displacement fields are given by the 3-D vector ( $\Delta x$ ,  $\Delta y$ ,  $\Delta z$ ). The east–west and north–south horizontal components,  $\Delta x$  and  $\Delta y$ , are incorporated into the tsunami source by the method proposed by Tanioka & Satake (1996), which combines the vertical component of the displacement vector with vertical changes induced by the interaction of horizontal displacement components and bathymetry gradients:

$$\Delta b = \Delta z - \Delta x \frac{\partial b}{\partial x} - \Delta y \frac{\partial b}{\partial y}, \quad (1)$$

where  $b = b(x, y)$  is the bathymetry (increasing in the upward direction). This contribution has been shown to be important both in general (e.g. Lotto *et al.* 2019) and for specific events, for example the 2011 Tohoku earthquake and tsunami (Murotani *et al.* 2015). However, for a physical model that includes flat bathymetry, the inclusion of horizontal displacement components has no effect on the tsunami source.  $\Delta b$  is time-dependent, since  $\Delta x$ ,  $\Delta y$  and  $\Delta z$  are time-dependent. The tsunami is sourced by adding  $\Delta b$  to the initial bathymetry and topography of the tsunami model.

The tsunami computational model is capable of accurately modelling gravity wave propagation as well as non-linear effects due to advection and shoaling. The fastest resolved waves in the hydrostatic tsunami model are gravity waves, characterized by their linear wave speed of  $v = \sqrt{gH}$ , where  $H$  is the mean water depth and  $g$  the gravitational acceleration constant. For the applications presented in Sections 3 and 4, the average water depth is 2000 m, thus, the maximum wave propagation speed is approximately 140 m s<sup>-1</sup>. Seismic surface waves in the earthquake rupture models are much faster, approaching approximately 2500 m s<sup>-1</sup>. These seismic surface waves feature large transient amplitudes of up to 1 m, which is of the same order as the static uplift at the end of the earthquake models. In nature, fast seismic surface waves at the elastic-acoustic interface are converted into infrasound or damped in the weakly compressible water column as the ocean response becomes non-hydrostatic at short wavelengths. However, seismic surface waves from an earthquake model may lead to spurious gravity waves in the tsunami shallow water approach. In addition, since a rupture model is not required to span the same spatio-temporal dimensions as the tsunami model, trailing seismic waves may show up as artefacts in final seafloor deformation. Thus, a space–time Fourier-transform based filter that removes unwanted signals from the tsunami source is applied.

### 2.3.2 Earthquake initial conditions

In the second example presented in Section 4, we initialize the earthquake model according to information from a subduction model

that extends the long-term geodynamic model of Gerya & Yuen (2007) to seismic cycles using seismo-thermomechanical models (van Dinther *et al.* 2013a,b, 2014). This 2-D subduction model solves for the conservation of mass, momentum and heat in an incompressible viscoelasto-plastic medium (Gerya & Yuen 2007, see Appendix C). After modelling millions of years of subduction, spontaneous frictional instabilities are simulated by reducing the time step combined with a strongly slip rate dependent friction law. Slip, stress and spatial characteristics of these frictional instabilities resemble those of natural earthquakes, albeit at very low slip rates (van Dinther *et al.* 2013a,b). We refer to these instabilities as ‘slip events’ to distinguish them from dynamic earthquake ruptures modelled with SeisSol, which capture frictional failure along a pre-existing fault and the accompanying seismic wave emissions.

To initialize the earthquake model using the subduction model, we port information from a single slip event following methods similar to those for initializing a 2-D earthquake model by van Zelst *et al.* (2019), but here extended to a 3-D earthquake model that is then linked to a tsunami model. We must pre-define a 3-D fault geometry in the earthquake model and do so by extending the 2-D fault that evolves during yielding in the subduction model in the third dimension. In addition, the material properties, stress state and friction coefficients from the 2-D slip event are extended into the third dimension in the earthquake model.

The computational subduction model is 2-D and assumes plane-strain. The 3-D computational earthquake model is not restricted to plane-strain conditions. We here extend the subduction model stress field into the third dimension for the earthquake model by setting the out-of-plane shear stresses to zero and the out-of-plane normal stress component to be a function of the two in-plane normal stresses and Poisson’s ratio  $\nu$ . Taking the in-plane coordinates from the subduction model as  $x$  and  $z$  and the out-of-plane coordinate as  $y$ , this is:

$$\begin{aligned} \sigma_{yy} &= \nu(\sigma_{xx} + \sigma_{zz}), \\ \sigma_{xy} &= 0, \\ \sigma_{yz} &= 0. \end{aligned} \quad (2)$$

We here adopt  $\nu = 0.5$ , which is the Poisson’s ratio used in the subduction model. This value arises from the assumption of incompressible rock, a valid assumption for modelling the long-term deformation at convergent margins.

Because the assumption of incompressible rock is not appropriate for dynamic earthquake rupture modelling, Poisson’s ratio must be reassigned to  $\nu < 0.5$  when transferring the material properties from the subduction model to the earthquake model. Lame’s parameter is then calculated from the assigned  $\nu$  and the shear modulus from the subduction model.

### 2.3.3 Data management in massively parallel simulations

The earthquake and tsunami computational models and their linkage requires input at several stages. For example, output from the subduction model is used to set the initial conditions for the earthquake model. Also, bathymetry data and seafloor displacements from the earthquake model are initial conditions in the tsunami model. To manage such data in massively parallel simulations, we use ASAGI (pArallel Server for Adaptive GeoInformation), an open-source library with a simple interface to access Cartesian material and geographic data sets (Rettenberger *et al.* 2016, [www.github.com/TUM-I5/ASAGI](http://www.github.com/TUM-I5/ASAGI)). ASAGI organizes Cartesian

data sets as a collection of tiles. For dynamically adaptive simulations, the parallel partitions that are assigned to each compute node may grow or shrink, as the mesh resolution is adapted. ASAGI automatically replicates or migrates the corresponding data tiles across compute nodes, which greatly simplifies the computing access to material or geographic data at a specific location.

### 3 TSUNAMIS SOURCED BY A BLIND VERSUS A SURFACE-BREACHING DYNAMIC RUPTURE

Here, we demonstrate methods and highlight key results for linking a generic 3-D megathrust rupture on a planar fault to tsunami generation and propagation in a basin with flat bathymetry and inundation on a linearly sloping beach. We compare tsunamis sourced by two earthquake scenarios that differ only by their near-surface fault strength, which controls the propagation of slip to the trench and results in one blind and one surface-breaching rupture.

We find that the surface-breaching rupture exhibits higher maximum and average fault slip and higher maximum and average vertical seafloor displacements. These differences are reflected in differing initial tsunami peak heights and wave shapes. However, the difference in peak height diminishes during tsunami propagation towards the beach and the inundation patterns are similar in both scenarios; inundation occurs along the same stretch of the beach and has the same run-up. The width of the inundated corridor inland from the coast and the timing of inundation do differ between scenarios, however, reflecting differences in timing in displacement of the water mass and in the magnitude of water displaced.

We can here study tsunami sensitivity to source time dependence, complementing heuristic findings (e.g. Davies 2019). By comparing these results to tsunamis sourced by the time-independent displacements, we find differences in the maximum run-up distances and in the temporal behaviour of the tsunami.

#### 3.1 Dynamic earthquake rupture model and scenarios

The earthquake physical model incorporates a planar fault that is 200 km along strike and extends from the surface to 35 km depth at a 16° dip. It intersects the seafloor and has an along-dip length of 127 km. The material around the fault is homogeneous with properties that reflect those estimated for oceanic crust in a subduction zone [density  $\rho = 3775 \text{ kg m}^{-3}$ , shear modulus  $G = 67.5 \text{ GPa}$ , Lamé parameter  $\lambda = 85.3 \text{ GPa}$ , from Stephenson *et al.* (2017)]. The computational mesh for this structural model has 16 million tetrahedral elements and coarsens gradually off the fault to a maximum mesh size of 100 km. A resolution of 66 m at the fault captures the dynamics in the process zone (Day *et al.* 2005) in which shear traction decreases from its static to its dynamic value just behind the earthquake rupture front (see Appendix B).

In this earthquake model, we use linear slip-weakening friction (Ida 1972). At any position on the fault, dynamic fault slip is modelled in two stages: first, there is static failure when the shear stress resolved on the fault exceeds the fault's static strength. Then, after failure, slip initiates, the fault weakens, and seismic waves are emitted. The static failure criterion is (using a compression negative sign convention):

$$|\tau_s| = c - \mu_s \tau'_n, \quad (3)$$

where  $\tau_s$  is the shear traction on the fault,  $\tau'_n$  is the effective normal traction,  $c$  is the on-fault cohesion and  $\mu_s$  is the static friction coefficient. The right-hand side in eq. (3) is the static fault strength.  $\tau'_n$  and  $\tau_s$  increase linearly with depth (Figs 2a and b) and we assign a uniform  $\mu_s$  of 0.275 (Fig. 2c). The effective normal traction includes the effect of pore fluid pressure, which we set to be depth-dependent and near-lithostatic ( $P_f = \rho_f gz$ , where  $\rho_f = -3000 \text{ kg m}^{-3}$ ,  $g$  is gravitational acceleration and  $z$  is depth, Fig. 2a).

The two earthquake scenarios that we compare here differ only by the static fault strength near the surface, controlled by  $c$  (Fig. 2d). In Scenario A,  $c = 0.4 \text{ MPa}$  everywhere below 15 km, but gradually increases above 15 km to 8 MPa at the top of the fault. In Scenario B,  $c = 0.4 \text{ MPa}$  everywhere.

We implement fault weakening in this model following the linear slip weakening friction law formulation proposed by Andrews (1976).  $\mu_s$  drops linearly to the dynamic coefficient of friction  $\mu_d = 0.25$  (Fig. 2c) over the slip weakening distance  $D_c = 0.5 \text{ m}$  (Fig. 2e). The earthquake rupture begins by forced weakening over time in a predefined patch following the nucleation procedure in several benchmarks from Harris *et al.* (2018). This nucleation patch is in the southeast corner of the fault at 26 km depth. Slip propagates spontaneously outward across the fault from this location for  $\sim 60 \text{ s}$  and is geometrically stopped at the three buried fault edges.

In Scenario A, the higher strength near the top of the fault smoothly stops the rupture as it approaches the surface, while in Scenario B, slip continues to the top of the fault and breaks the surface. Fig. 3 shows the accumulated fault slip as well as the final and maximum vertical surface displacements for both scenarios.

Key earthquake characteristics for the blind (Scenario A) and surface-breaching (Scenario B) ruptures are compared in Table 1. The surface-breaching rupture results in a comparable moment magnitude ( $M_w 8.6$ ) to the blind rupture ( $M_w 8.5$ ), while the average dynamic stress drop is 3.9 MPa in the surface breaching rupture and 3.0 MPa for the blind rupture. In distinction, the average and maximum accumulated fault slip are considerably lower in the blind rupture, at 3.8 and 7.6 m, while the surface-breaching rupture has average slip of 6.5 m and maximum slip of 10.9 m. The fault slip is also differently distributed: the surface-breaching rupture presents large shallow slip, whereas the peak slip occurs deeper in the blind earthquake scenario.

In both earthquakes, the average rupture velocity resembles a typical megathrust tsunamigenic earthquake, but not a slower ‘tsunami’ earthquake Kanamori (1972). The mean values are similar in both scenarios, at  $3.5 \text{ km s}^{-1}$  for the blind rupture and  $3.7 \text{ km s}^{-1}$  for the surface-breaching rupture. Rupture velocity remains subshear relative to the  $4.3 \text{ km s}^{-1}$  S-wave speed in the surrounding material along most of the fault during the blind rupture, but transitions locally to supershear speed up-dip from the nucleation location and along the upper part of the fault in the surface-breaching rupture.

For both earthquake scenarios, the maximum and minimum vertical seafloor displacements over the entire earthquake occur at  $t = 56 \text{ s}$ . In the blind rupture, these are 2.6 and  $-1.0 \text{ m}$ , respectively. For the surface-breaching rupture, the maximum is larger at 3.3 m, but the minimum is comparable at  $-1.1 \text{ m}$ . The average vertical displacement at this time is 0.6 m for the blind rupture and twice as large, at 1.2 m, for the surface-breaching event. The displacements continue to change after this time in both scenarios until they reach constant values. For the blind rupture, this occurs at  $\sim t = 80 \text{ s}$ , when spatial maximum is 1.9 m, the minimum is  $-1.0 \text{ m}$

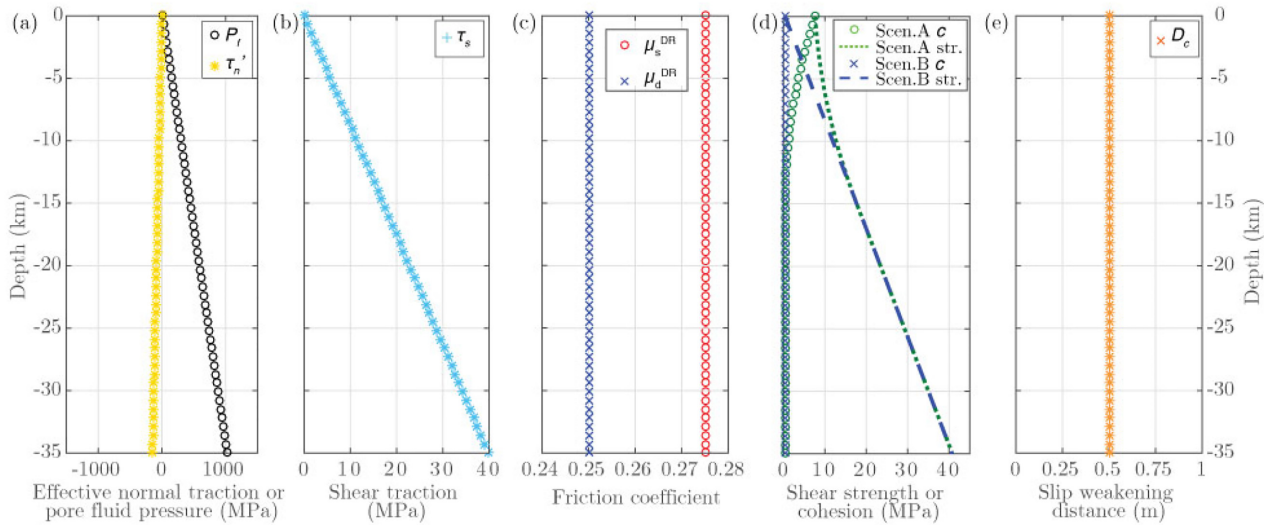


**Figure 2.** Parameters for the blind and surface-breaching earthquakes in Scenarios A and B (detailed in Section 3) along a cross section at  $y = 0$  through the 3-D fault: (a) effective normal traction and pore fluid pressure, (b) shear traction, (c) coefficients of static and dynamic friction, (d) on-fault cohesion and fault strength, and (e) slip-weakening distance. Only the cohesion (shown in d) along the shallow fault differs from Scenario A to Scenario B.

and the average is 0.9 m. For the surface-breaching rupture, this occurs later at  $\sim t = 95$  s, when the spatial maximum is 2.6 m and the minimum is  $-1.2$  m. However, the average final displacement is 0.9 m, which matches that for the blind rupture. In both scenarios, surface waves continue to propagate until the predefined end of the model run, which is set to  $t = 120$  s for the blind rupture and at  $t = 124$  s for the surface-breaching rupture.

### 3.2 Tsunami propagation and inundation model and scenario

The tsunami physical model includes a flat seafloor and a linearly sloping beach (Fig. 4). Hence, we define the bathymetry by

$$b(x, y) = \begin{cases} 0.05(x - x_0) & \text{for } x > x_0 \\ 0 \text{ km} & \text{otherwise,} \end{cases} \quad (4)$$

where  $x_0 = 200$  km is the beach toe, where the slope begins. The initial sea surface is flat ('sea-at-rest') and located at  $z = 2$  km, which means that the coastline is located at  $x = 240$  km. Above this level, the water depth is set to zero. We refer to the sea surface height ( $ssh$ ) as the deviation from the reference height of 2 km. The model domain, which ranges from  $x = -400$  to 400 km and from  $y = -400$  to 400 km, is set to be larger than the horizontal extent of the earthquake physical model to minimize model boundary effects. The minimum mesh size is 12.2 m.

The bathymetry perturbation field  $\Delta b$  (eq. 1), accounting for the time-dependence of the simulated displacement field, is used to initiate the tsunami model. The unstructured output from the earthquake model is bilinearly interpolated to an intermediate uniform Cartesian mesh with a resolution of 1000 m, which is used for the transfer between models. We also apply a space–time Fourier filter to remove unwanted signals from the tsunami source that are present in the output from the earthquake model (Section 2.3.1). This filtering approach is further discussed in Section 5.1. Fig. 4 shows  $\Delta b$  at  $t = 102$  s.

Snapshots of the simulated tsunami wave-field are shown in Fig. 5. Also, key characteristics of the tsunami sourced by the blind rupture (Scenario A) and the surface-breaching rupture (Scenario B) are summarized in Table 2.

Maximum initial  $ssh$  resembles the maximum coseismic seafloor uplift of 2.6 m from the blind rupture and 3.3 m from the surface-breaching rupture. As shown in Fig. 6, the (filtered) source displacements of the blind rupture in Scenario A produce a smooth wave while those in Scenario B produces more abrupt initial displacements of the water column, as discussed in Section 5.1. The cross-section at  $y = 0$  and  $t = 120$  s in Fig. 6(a) shows that the wave peak is initially higher for the surface-breaching rupture source. At  $t = 1200$  s, just before first inundation in both scenarios, the heights of the peaks nearest the beach are more similar (Fig. 5b). For the blind rupture source, the tsunami reaches a maximum of  $ssh = 3.0$  m at  $t = 1470$  s, while for the surface-breaching rupture source, the tsunami reaches  $ssh = 3.4$  m at  $t = 1480$  s, a difference of 0.4 m. By  $t = 1600$  s, the approximate time of maximum inundation, differences in peak heights have diminished, while tsunami wave distribution still differs (Fig. 5c).

We track the wave heights on land by comparing time series at 10 km inland from the coast near  $x = 240$  km along cross-sections at  $y = -150, 0$  and 150 km (Fig. 4d). The highest wave height occurs at  $y = 0$  km in both Scenario A and Scenario B. However, the wave heights are asymmetric due to the uni-directional earthquake ruptures. Higher waves occur at  $y = 150$  km, the part of the coast that is closer to locations of larger fault slip and uplift in both earthquake scenarios. Lower waves occur at  $y = -150$  km, the part of the coast that is closer to the earthquake hypocentre. The height of the tsunami wave at the coast from the blind rupture is 0.8 m higher than the maximum wave height near the source, though this difference is only 0.1 m for the tsunami sourced by the surface-breaching rupture (Table 2).

In general, wave peaks in Scenario B appear delayed relative to peaks in Scenario A, which is at least partially due to the fact that the location of highest seafloor displacement is farther away from the coast in Scenario B. This delay is more pronounced at  $y = 150$  km and  $y = -150$  km than at  $y = 0$  km (Fig. 4d), where it is approximately 100 s. The average velocity from  $t = 1000$  s to  $t = 1100$  s of the wave peak from blind rupture source in Scenario A is  $157 \text{ m s}^{-1}$ , faster than that for the surface-breaching rupture source in Scenario B of  $142 \text{ m s}^{-1}$ . This is in contrast to the earthquake

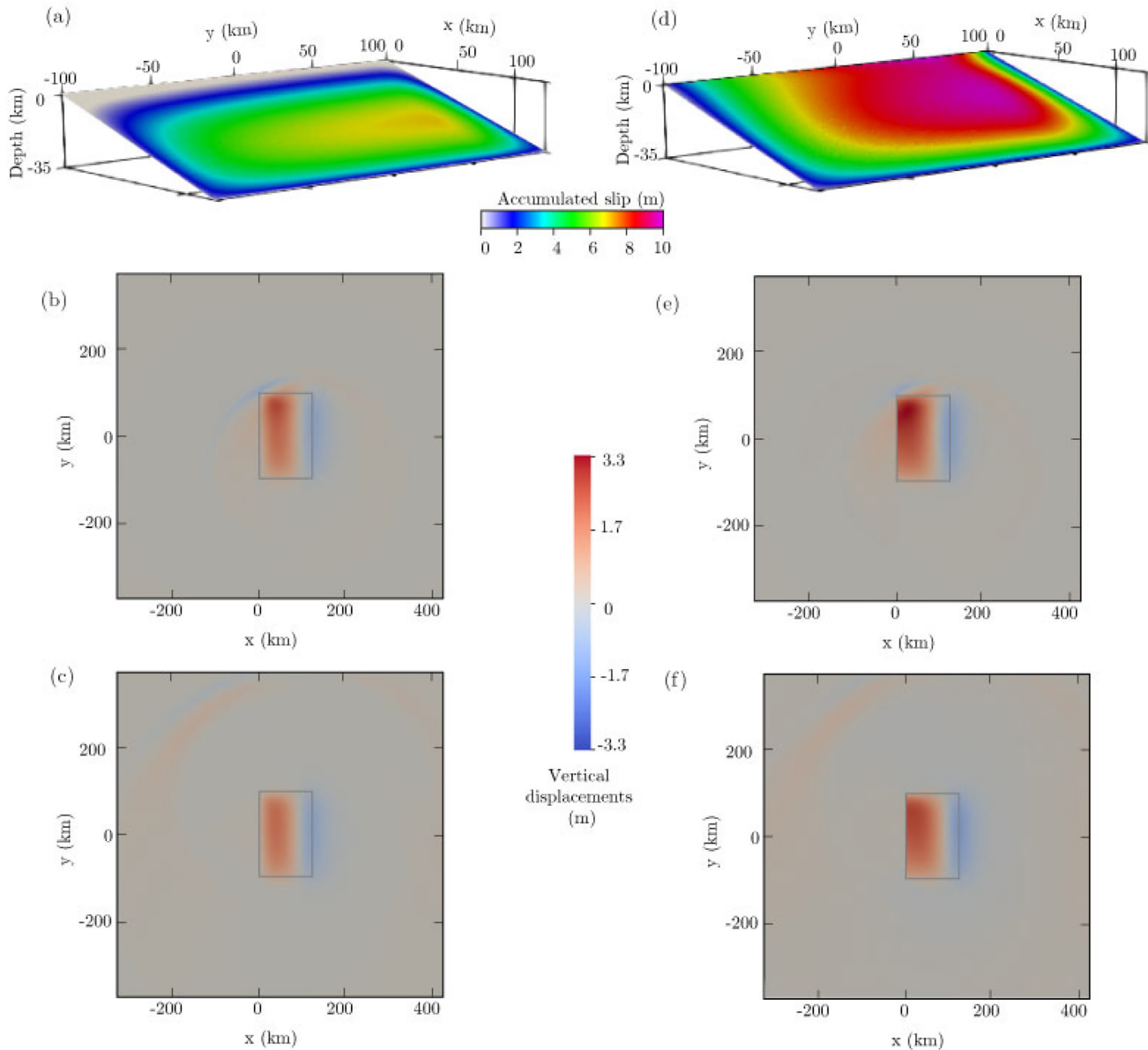


**Figure 3.** Blind versus surface-breaching earthquake scenarios. Scenario A (blind rupture): (a) accumulated slip, (b) vertical surface displacements at 56 s (time of maximum uplift) and (c) final vertical displacements. Scenario B (surface-breaching rupture): (d) accumulated slip, (e) vertical surface displacements at 56 s (time of maximum uplift) and (f) final vertical displacements.

**Table 1.** Earthquake model results. Characteristics for the blind (Scenario A), surface-breaching (Scenario B) and subduction-initialized (Scenario C) dynamic earthquake rupture models.

	$M_w$ (-)	max. $s^a$ (m)	Mean $s$ (m)	Mean $V_r^b$ ( $\text{km s}^{-1}$ )	mean $\Delta\sigma^c$ (MPa)	min. D $d$ (m)	max. D (m)	Mean D (m)	max. D $e$ (m)	Mean D $f$ (m)
Scenario A	8.5	7.6	3.8	3.5	3.0	-1.0	2.6	0.6	1.9	0.9
Scenario B	8.6	10.9	6.5	3.7	3.9	-1.1	3.3	1.2	2.6	0.9
Scenario C	9.0	95.5	42.2	2.1	2.2	-5.6	28.1	3.6	15.7	3.3

Note: <sup>a</sup>Slip.

<sup>b</sup>Rupture velocity.

<sup>c</sup>Dynamic stress drop.

<sup>d</sup>Vertical displacement.

<sup>e</sup>Vertical displacement at end of earthquake model.

rupture speed, which is on average faster in Scenario B and features supershear episodes.

The difference in propagation velocity does not affect the time of first inundation, which occurs at almost the same time in Scenario

A ( $t = 1210$  s) and Scenario B ( $t = 1220$  s, Table 2). Inundation maps for both scenarios are shown in Figs 7(a) and (b). In both scenarios, the waves reach a maximum runup of 73 m at the centre of the beach (near  $y = 0$ ). Away from the centre, the run-up is lower.

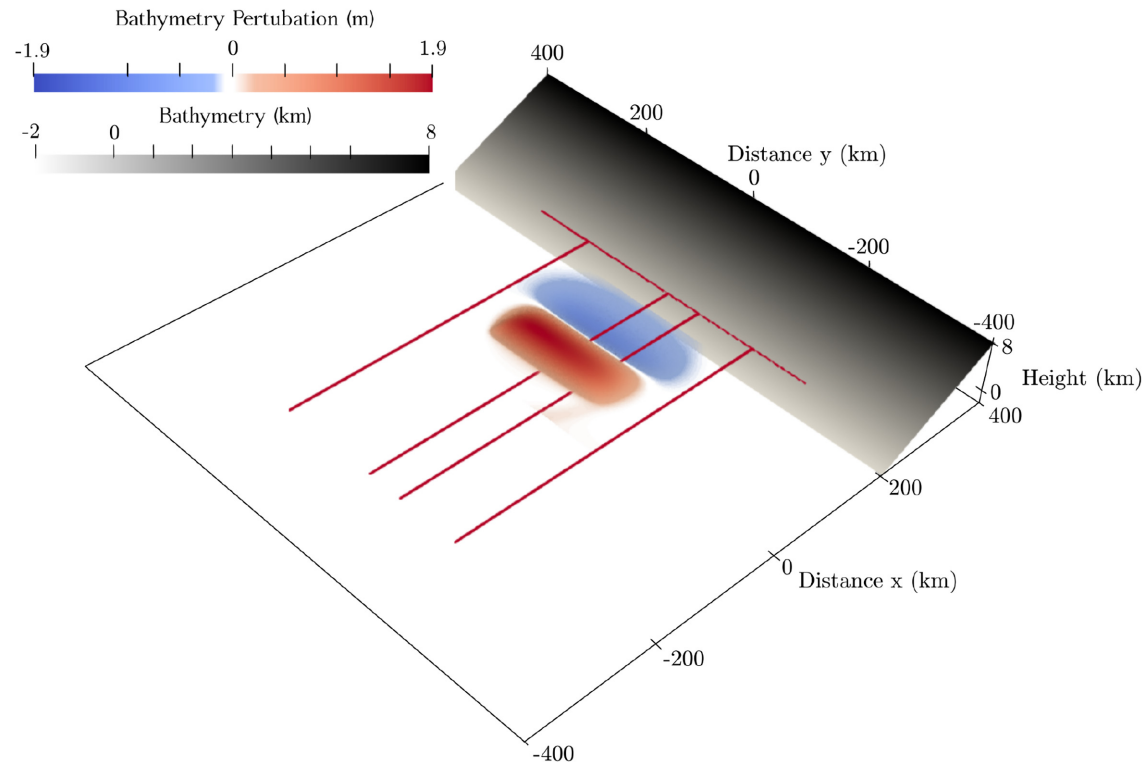


**Figure 4.** Bathymetry (flat seafloor and a linearly sloping beach) and bathymetry perturbation [ $\Delta b(t, x, y)$ ] used in the tsunami model from the Scenario A blind earthquake at  $t = 102$  s. Red are cross-sections at  $y = -150.0, -55, 0, 150.0$  km and measurement points along the beach at  $x = 240.0$  km.

The inundation area is slightly asymmetric and skewed towards  $y = 150$  km in both scenarios.

Fig. 7(c) shows that, even though the first arrival occurs at approximately the same time, inundation in Scenario B is delayed near the coast and laterally along the coast by up to 100 s relative to Scenario A. This is probably due to the delay in the wave peak in Scenario B (relative to Scenario A) shown in Fig. 4(d) and the faster wave propagation speed in Scenario A. In contrast, inundation at locations farther inland from the coast occurs earlier in Scenario B by approximately 60 s. The final inundated area for the surface-breaching rupture in Scenario B ( $18.3 \text{ km}^2$ ) is 15 per cent larger than for the blind rupture in Scenario A ( $15.6 \text{ km}^2$ ). The differences occur inland from the coast, where Scenario B inundates a wider corridor.

### 3.2.1 Comparison to tsunamis sourced using the time-independent displacements

We now compare the tsunamis from both scenarios when the time-independent filtered displacements from the end of the earthquake model are used in the sources instead of the time-dependent displacements from throughout the dynamic earthquake rupture scenario. The time-independent seafloor uplift has a maximum of 1.9 m for the blind rupture in Scenario A versus 2.6 m for the surface-breaching rupture in Scenario B. This is lower than the maximum uplift during the entire earthquake at  $t = 100$  s of 2.6 and 3.3 m in these scenarios, respectively (Table 1). However, the average time-independent displacements are equivalent at 0.9 m for both scenarios.

In general, the tsunamis from the time-independent sources inundate the coast earlier than those from the dynamically sourced models. To compare them, we equalize the times of first inundation:

the time-independent source from the blind rupture in Scenario A is shifted by 40 s and the source from the surface-breaching rupture in Scenario B by 60 s. Figs 7(d) and (e) show the inundation corridors. These are best analysed by looking at their differences to other results. The similarity of Fig. 7(f) with Fig. 7(c) suggests that the differences between the two scenarios are unaffected by the change from a time-dependent to a time-independent source.

Figs 7(g) and (h) show the differences between tsunamis for each scenario with the change in the source. Importantly, in the surface rupturing Scenario B, the maximum run-up distance near  $y = 0$  is overpredicted with the time-independent source (Figs 7e). In other characteristics, the two scenarios respond in a similar way to this change in source. The waves from the time-independent source arrive later at the coast along  $y < 0$  and earlier at the coast along  $y > 0$ . So, coastal inundation occurs over a shorter time. This is consistent with the source from a single time-step, rather than over the entire lifetime of the earthquake rupture. Farther inland, this trend is less pronounced. These differences in wave timing are visible in (Fig. 8) as well, which shows that the tsunamis from time-independent sources lag behind those from the time-dependent sources at  $y = 0$  km and precede the time-dependent sources at  $y = 150$  km. The tsunami from the time-independent sources also over predict wave height at  $y = 0$  km.

### 3.3 Conclusion

Using our virtual laboratory, we simulate tsunamis sourced by two megathrust earthquake scenarios that differ only by their near-trench fault strength and, as a result, slip behaviour. This results in one blind and one surface-breaching rupture that differ in fault slip distribution and rupture kinematics. The surface-breaching rupture exhibits

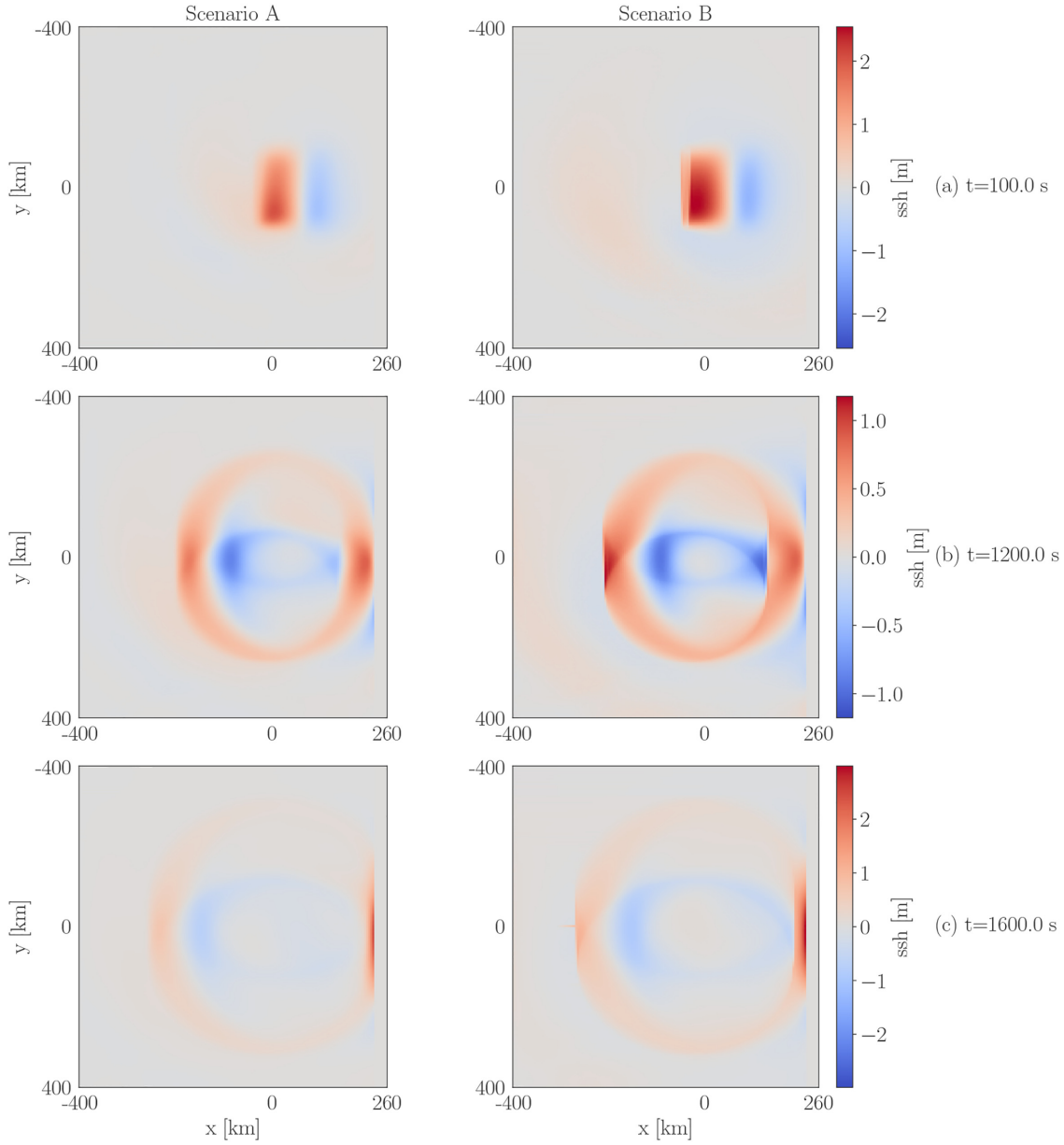


**Figure 5.** Sea surface height (ssh) in the tsunami sourced by the blind (Scenario A) and surface-rupturing (Scenario B) earthquakes (detailed in Sec. 3) at (a, first row) the final time of the earthquake model, (b, middle row) the approximate time of the first inundation and (c, last row) the approximate time of maximum inundation.

**Table 2.** Tsunami model results. Characteristics for tsunamis sourced by the blind (Scenario A), surface-breaching (Scenario B) and subduction-initialized (Scenario C) dynamic earthquake rupture models.

	max. ssh (t) <sup>a</sup> (m)	time of first in. <sup>b</sup> (s)	max. ssh at coast (t) (m)	max. runup (t) (m)	total in. <sup>b</sup> area (km <sup>2</sup> )	wave speed <sup>c</sup> (m s <sup>-1</sup> )
Scenario A	2.6 (56 s)	1210	3.4 (1470s)	73 (1450 s)	15.6	157
Scenario B	3.7 (56 s)	1220	3.75 (1480s)	73 (1400 s)	18.3	142
Scenario C	28.1 (100 s)	2050	24.3 (2520s)	492 (2410 s)	27.2	148

Note: <sup>a</sup>maximum sea surface height at time (*t*).

<sup>b</sup>Inundation.

<sup>c</sup>Propagation speed calculated for wave peak at *y* = 0 from *t* = 1000 to *t* = 1100 s, the time of first inundation.

70 per cent larger average fault slip and 40 per cent larger peak fault slip. Despite this, the surface-breaching rupture causes a maximum seafloor displacement that is only 35 per cent higher than the blind rupture and the spatial averages of the seafloor displacements at

the end of both earthquake scenarios are equal. The difference in maximum displacement is reflected in different initial tsunami peak heights, but this difference diminishes during tsunami propagation towards the beach and at the time of maximum inundation at the

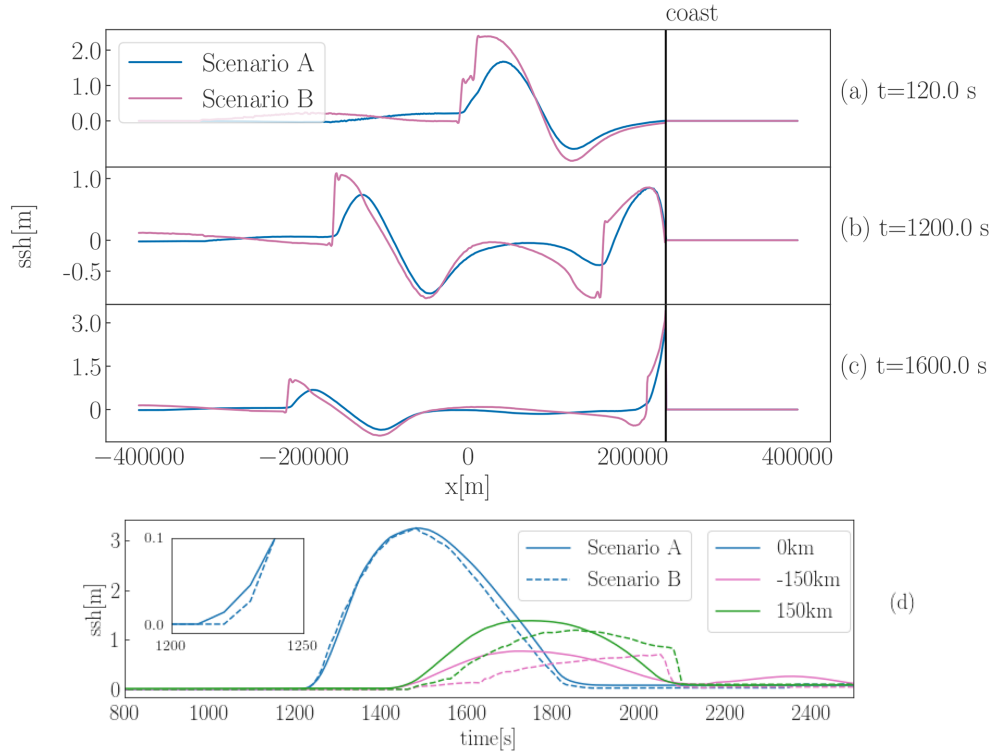


**Figure 6.** Sea surface height (ssh) in the tsunami sourced by the blind (Scenario A) and surface-rupturing (Scenario B) earthquakes (detailed in Section 3) along a cross section at  $y = 0$  km and at (a) the final time the earthquake model, (b) the approximate time of the first inundation and (c) the approximate time of maximum inundation. (d) Time series of ssh at 3 points located 10 m from the coast near  $x = 240$  km for Scenario A and Scenario B.

coast at  $y = 0$  km, the peak wave height differential is only 0.4 m. The tsunamis in both scenarios flood asymmetric regions due to the unidirectional earthquake rupture and inundate the same 400 km of the coast and exhibit the same run-up of 73 m. However, the tsunami generated by the surface-breaching rupture inundates a 15 per cent larger area overall due to a wider inundation corridor inland from the coast.

For both scenarios, using the time-independent displacements in place of the time-dependent displacements in the tsunami source results in later arrival at the coast, but faster coastal inundation. For the surface-breaching rupture source, using the time-dependent displacements also overpredicts run-up.

#### 4 TSUNAMI SOURCED BY A SUBDUCTION-INITIALIZED DYNAMIC RUPTURE

We now use output from a 2-D subduction model (Section 2.3) to build the 3D earthquake model (Scenario C). In this way, earthquake initial conditions are assigned self-consistently and the tsunami source reflects the conditions developed over long-term subduction and seismic cycling. This adds complexity to the earthquake source relative to scenarios A and B in the previous section.

The earthquake initial conditions are heterogeneous and characterized by stark material contrasts, for example between sedimentary and basaltic regions, as well as smaller scale heterogeneous conditions reflected in fault geometry, fault strength, friction drop and stresses. Pore fluid pressure is elevated at a ratio of 0.95 to the lithostatic stress. Also, the critical slip weakening distance  $D_c$  here

varies with depth to resemble the friction drop measured during the geodynamic slip event.

We use the same methods as in Section 3.2 to link the earthquake model to the tsunami model. The fault does not intersect with the surface, so the rupture is blind, but it efficiently generates a tsunami.

#### 4.1 Dynamic earthquake rupture

##### 4.1.1 Earthquake physical model

We initialize the dynamic rupture model by porting the fault geometry and strength, material properties and stress state from one slip event in the subduction model. Both the geodynamics and seismic cycling phases of the subduction model and the definition of a slip event are described in Appendix C. The workflow for linking subduction to a 3-D earthquake model is detailed here, which expands the approach for a 2-D earthquake presented in van Zelst *et al.* (2019).

The sides of the earthquake physical model are 1600 km and it extends to 500 km depth (Fig. 9a). The fault from the subduction slip event is a curve that extends for 320 km in the fault dip direction to a depth of 100 km. Fault dip gradually increases with depth, ranging from  $2.3^\circ$  to  $34^\circ$  and averaging  $14.8^\circ$ . To pre-define the 3-D fault in the earthquake model, fault locations are taken from the subduction slip event every 500 m in the  $x$ -direction (distance from trench) at the depth ( $z$ -direction) of the maximum strain rate over the entire slip event and smoothed with a moving average filter. To expand this line to a 3-D fault surface, we assume that it is uniform in the third dimension, along fault strike, and extend it for 400 km (Fig. 9a). The fault does not intersect the surface, neither in the subduction

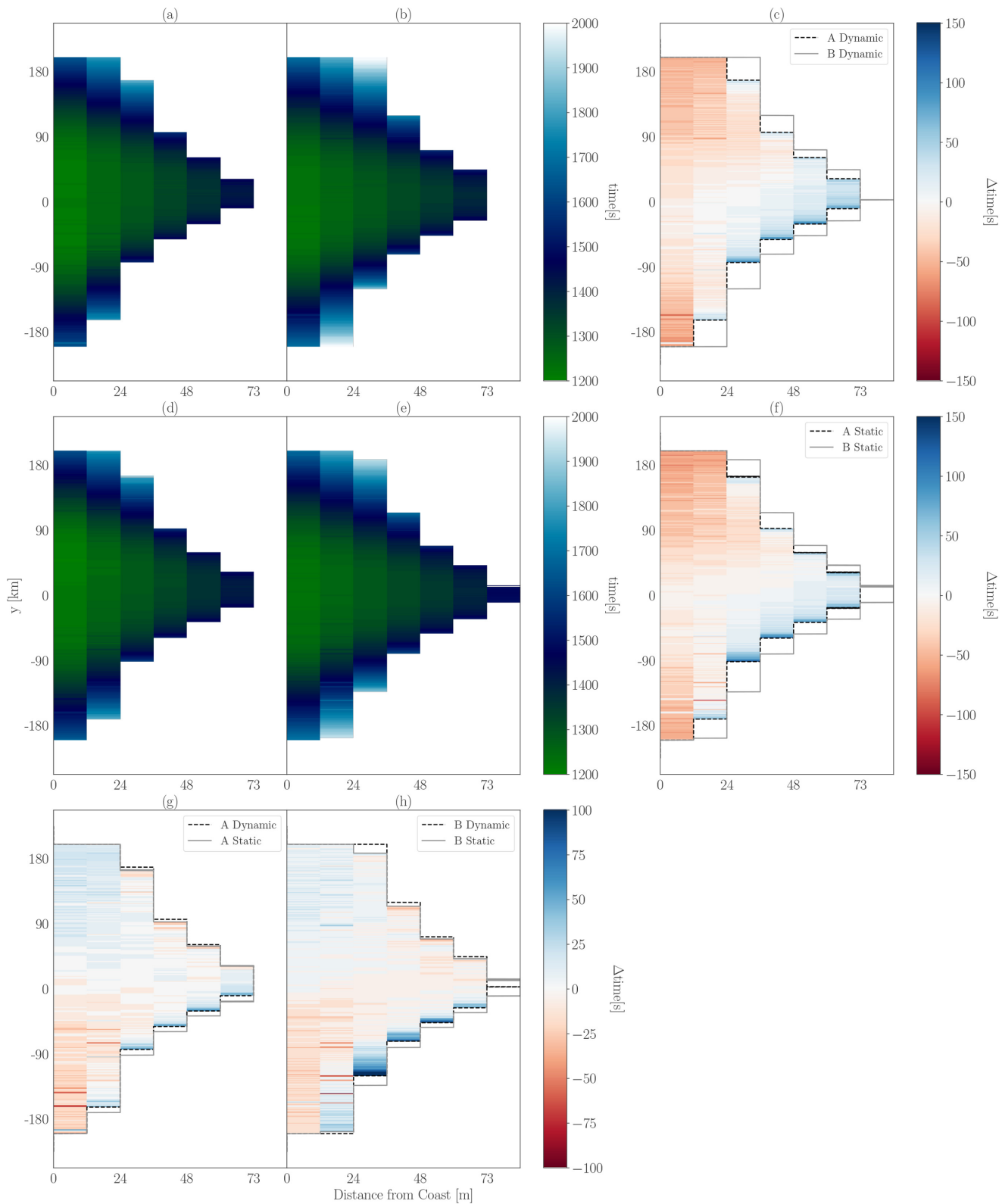


**Figure 7.** Inundation for Scenario A (blind earthquake rupture, first column) and Scenario B (surface-breaching rupture, second column) (see Section 3), incorporating the time-dependent (dynamic) filtered seafloor displacements (first row) or the time-independent (static) displacements (second row). The third column shows temporal differences between inundation in scenarios A and B, with negative values indicating that Scenario B's tsunami waves arrive later. The third row shows temporal differences between inundation from the time-dependent and time-independent sources, with negative values indicating that the waves from the time-independent source arrive later. The coast is located at  $x = 240$  km. The stepwise inundation distribution reflects the spatial mesh discretisation near the coast.

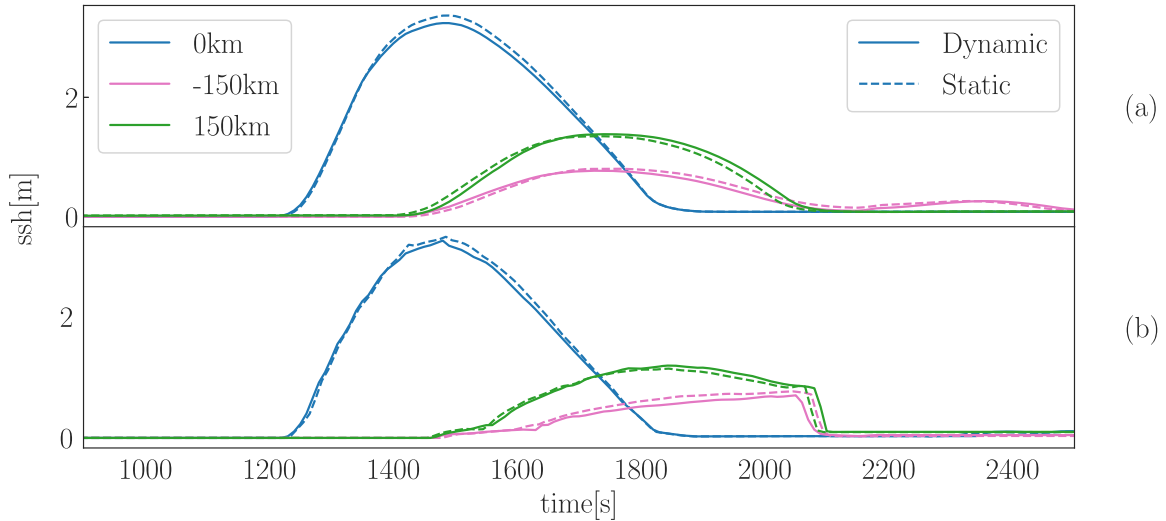


**Figure 8.** Time series of sea surface height (ssh) at 3 measurement points located 10 m from the coast near  $x = 240$  km for tsunamis sourced by the time-dependent and time-independent filtered displacements from (a) the blind rupture in Scenario A and (b) the surface-breaching rupture in Scenario B.

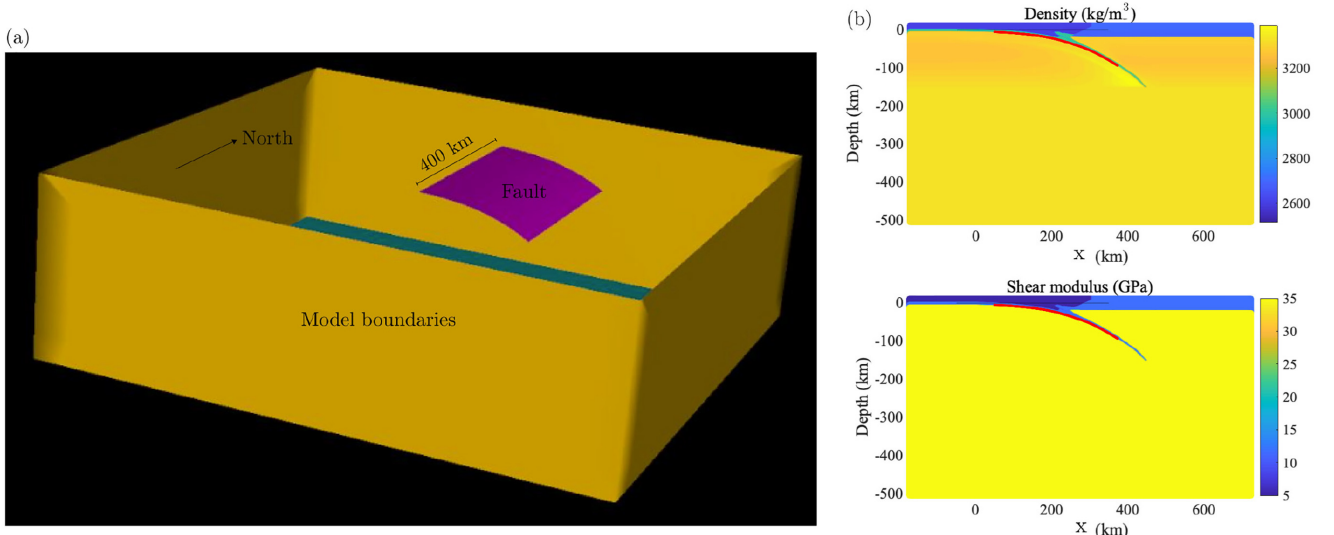


**Figure 9.** (a) Structure of the earthquake model for the subduction-initialized earthquake in Scenario C (see Section 4.1.1). Volume (yellow) is 1600 km along each side and 500 km deep. Fault (pink) is 400 km along strike. (b) Material properties. Red curve shows fault that evolves during the subduction slip event. Lame's parameter is equal to the shear modulus shown here.

nor earthquake models. We spatially discretize this structural model with elements of an edge length of 1 km on the fault, 5 km within a mesh refinement zone surrounding the fault, and a maximum element edge length of 20 km (Appendix B and Fig. A1).

The material properties and stress state are taken from the start of the subduction slip event (Fig. A2). As discussed in Section 2.3, the material properties for the earthquake model are determined by reassigning Poisson's ratio, here to  $\nu = 0.25$ . This results in a Poisson solid with Lame's parameter equal to the shear modulus ( $\lambda = G$ ). The material properties used in the earthquake model are shown in a slice through the 3-D volume in Fig. 9(b). These are applied uniformly in the third dimension, along fault strike, in the earthquake model. The Cartesian stresses are ported to the earthquake model and stress in the third dimension (parallel to fault strike) is set by honoring the plane-strain assumption taken in the subduction model (Section 2.3).

In the earthquake model, fault failure occurs according the stress resolved on the fault as:

$$|\tau_s| = c - \mu'_s \tau_n. \quad (5)$$

This is equivalent to eq. (3), but expressed in terms of the absolute normal traction,  $\tau_n$ , and the effective static coefficient of friction,  $\mu'_s$ , at the beginning of the subduction slip event. We use the term effective here because  $\mu'_s$  accounts for the pore fluid pressure, which has a ratio to the lithostatic stress of 0.95 along the fault during this slip event.  $\tau_n$  increases with depth, while  $\tau_s$  reaches a maximum near 43 km depth and minima near the surface and at large depths (Figs 10a and b). We assign the frictional cohesion,  $c$ , to equal the bulk cohesion,  $C$ , in the subduction slip event (Fig. 10d). We do, however, increase  $c$  in the earthquake model along the part of the fault that cuts through the sediments, as discussed at the end of this

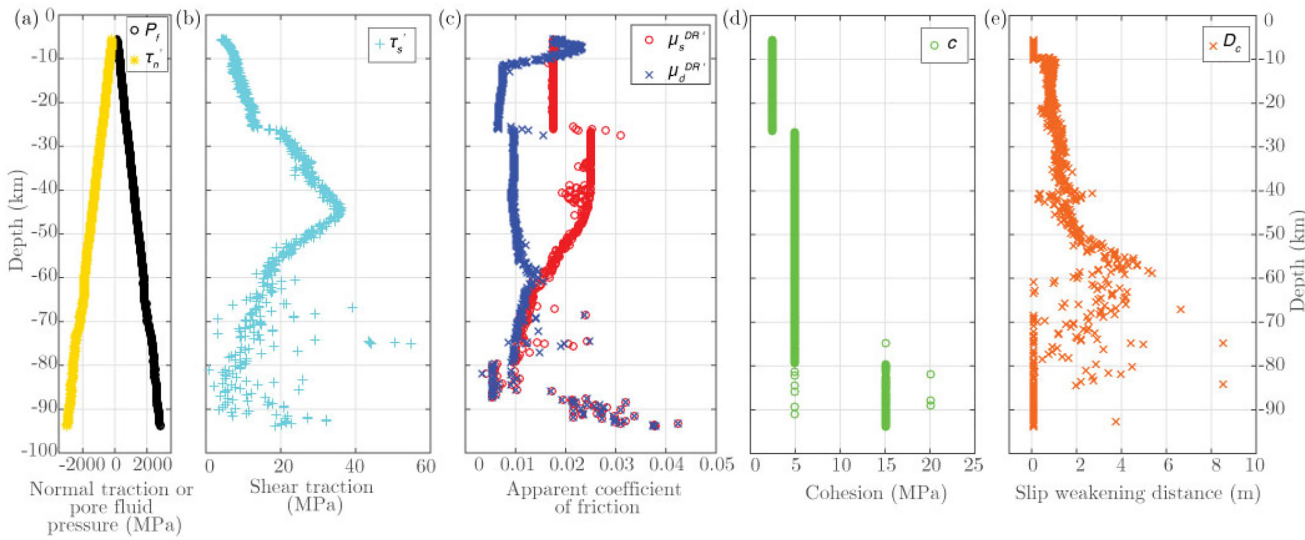


**Figure 10.** Initial conditions along a cross section at  $y = 0$  through the 3-D fault used in the subduction-initialized earthquake in Scenario C before corrections are made to  $c$  in the sediments above approximately 25 km depth and to  $\mu_s$  at outliers (see Section 4.1.1): (a) normal traction and pore fluid pressure, (b) shear traction, (c) effective static and dynamic friction coefficients, (d) on-fault cohesion and (e) slip-weakening distance.

section. The Cartesian stress tensors are initialized in the earthquake model and SeisSol determines the tractions on the fault. Hence, it is critical that the fault and stresses in the earthquake model are in the same location relative to one another as in the subduction model (Appendix D).

After the onset of failure, the earthquake model fault weakens according to a linear slip-weakening friction law (Andrews 1976) and  $\mu'_s$  changes with slip to an effective dynamic value,  $\mu'_d$ . If the fault location is in a velocity strengthening region of the subduction model, we assign  $\mu'_d$  to equal the maximum effective friction reached at that location during the entire subduction slip event, which may be locally larger than  $\mu'_s$ . If the fault location is in a velocity weakening region, we assign  $\mu'_d$  to equal the minimum value effective friction reached at that location during the entire subduction slip event. The 2-D slip weakening distance,  $D_c$ , is assigned such that the friction drop is equivalent to that along the 1-D fault in the subduction slip event (van Zelst *et al.* 2019). As shown in (Fig. 10e), such constrained  $D_c$  varies with depth.

In a pre-modelling step taken before running the earthquake model, we check for points of static failure according to the earthquake model criterion (eq. 5) along a cross-section through the 3-D fault shown in Fig. 11. The failure criterion is met in three locations: within the shallow sediments, at one isolated point at 74.7 km depth, and in the region of 40–43 km depth.

In the subduction model, the slip event spontaneously initiates at 40–43 km depth. This is a location where the correct brittle failure mechanisms also are active. We predefine 3-D a nucleating patch here in the earthquake model centred at  $x = 267$  km,  $y = 0$  km and  $z = -41.5$  km and with a radius of 1.3 km. Inside the patch we assign  $\mu'_s = 0.019$ , equal to the minimum value of  $\mu'_s$  in the subduction model inside this nucleating region. In order to restrict nucleation laterally, we then set  $\mu'_s = 0.025$  in the regions outside of, but at the same depths as, the nucleation zone. This is the value of  $\mu'_s$  above 40 km depth. We discuss linkage related to nucleation further in Section 5.2.

In the subduction model, nucleation of a slip event in the shallow sediments and at 74.7 km depth is inhibited. The shallow sediments are always at plastic failure, but velocity strengthening allows continuous creep through time without nucleation of brittle failure.

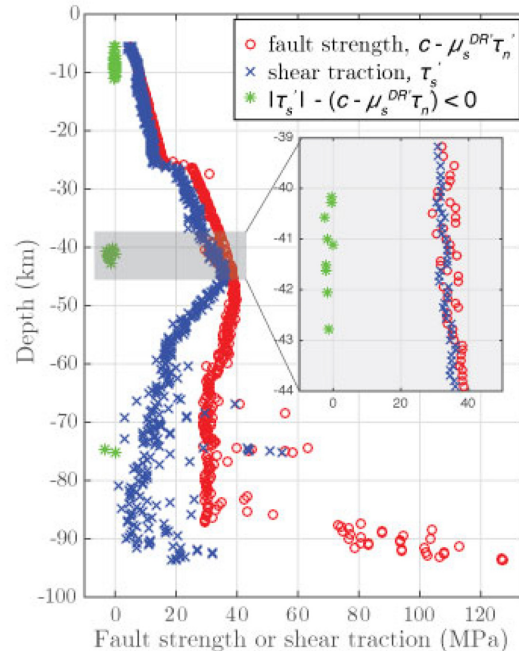


**Figure 11.** (a) Failure analysis according to the earthquake model failure criterion (eq. 3) at points along a cross section at  $y = 0$  through the 3-D earthquake model fault in Scenario C. Green stars are locations initially at failure, before adjustments are made to prevent such failure in the sediments and at outliers (see Section 4.1.1). Zoom is to the region near the nucleation zone.

However, localized exceeding of the failure criterion in the earthquake model would lead to rupture nucleation. Therefore, we prevent failure by assigning  $c = 5$  MPa in the sediments above 25 km depth, which is the value of  $c$  in the deeper basalt.

At 74.7 km depth, high temperatures ensure deformation occurs predominantly through dislocation creep in the subduction model. Again, isolated exceeding of the failure criterion in the earthquake

model leads to rupture nucleation here. To prevent this, we assign  $\mu'_s = 0.02$ , which is the value of  $\mu'_s$  nearby.

We make one minor, additional adjustment to the earthquake model. Near the material contrast at 27 km depth,  $\mu'_s$  and  $\mu'_d$  are anomalously large due to interpolation inaccuracies near stark material contrasts (Fig. 10c). We relax  $\mu'_s$  and  $\mu'_d$  at these points to the values of material below, such that  $\mu'_s = 0.025$  and  $\mu'_d = 0.0097$ .

#### 4.1.2 Earthquake rupture scenario

This subduction-initialized earthquake in Scenario C initiates spontaneously within the nucleation patch due to the locally high  $\tau_s$  and locally low  $\mu'_s$  inherited from the 2-D subduction slip event (Fig. 11). Slip then progresses outward in all directions along the fault, producing a  $M_w$  9.0 earthquake with an average dynamic stress drop of 2.2 MPa, which is lower than in Scenarios A and B (Section 3). The rupture does not progress to the shallowest or deepest parts of the fault due to the stress and strength conditions there and is stopped by the fault edges along the central fault. The accumulated fault slip reaches maxima of 95.5 m in two locations, as shown in Fig. 12(a), and the average accumulated slip is 42.2 m, which is higher than in Scenarios A and B. Slip prevails for approximately 150 s. Waves continue to propagate after this time and surface waves and waves trapped in the sediments are still present at the end of the earthquake scenario at  $t = 241$  s (Figs 12b and c). The large modelled slip results from the effect of reverberating seismic waves and the chosen Poisson's ratio, similar to the 2-D case (van Zelst *et al.* 2019).

The S-wave speed for the basalt around the fault is  $3.2 \text{ km s}^{-1}$ . The earthquake rupture velocity exceeds this locally, reaching supershear speeds near the nucleation location and laterally along the fault at the depth of nucleation. Elsewhere along the fault, the rupture proceeds at subshear speeds. On average, the rupture velocity is  $2.1 \text{ km s}^{-1}$ , which is slower than the average velocities of the ruptures in Scenarios A and B, but still higher than a 'tsunami' earthquake Kanamori (1972).

The maximum vertical surface displacement over the entire earthquake is 28.1 m and occurs at  $t = 100$  s (Fig. 13). At this time, the minimum vertical displacement is  $-5.6$  m and the average is 3.6 m. After the earthquake simulation ends at  $t = 241$  s (Figs 12b and c), the maximum and minimum displacements are 15.7 and  $-6.7$  m, respectively, and the average is 3.3 m. All characteristic displacements are larger than in Scenarios A and B (see Table 1).

#### 4.2 Tsunami propagation and inundation

The tsunami physical model in Scenario C is the same as that used in Section 3.2, but its spatial dimensions are adjusted to the larger earthquake model. The beach slope begins at  $x_0 = 500$  km, the coast is located at  $x = 540$  km, and the size of the domain extends from  $x = -600$  to 600 km and  $y = -600$  to 600 km (Fig. 13). As in Section 3.2, the tsunami source,  $\Delta b$ , incorporates the time-dependent 3-D seafloor displacements from the earthquake scenario following eq. (1). The unstructured output from the earthquake model is bilinearly interpolated to a structured mesh at a resolution of 1000 m. As previously done, we apply a space-time Fourier filter to  $\Delta b$  which is discussed in Section 5.1.

The seafloor displacements are symmetric about the  $x$ -axis during the entire earthquake (Figs 12c and 13), as expected based on the symmetrically centred nucleation region. Figs 14(a)–(d) shows the field of the sea surface height ( $ssh$ ) for different moments in time. Initially,  $ssh$  reflects the vertical displacement magnitudes from the

earthquake (Fig. 14a), then the tsunami develops a circular wave propagating away from the source (Fig. 14b) until it reaches the coast at  $t = 2050$  s. At this time, the wave at  $y = 0$  reaches  $ssh = 24$  m, 0.4 m lower than the maximum height near the earthquake source, but much higher than in Scenarios A and B (Table 2). Fig. 14(c) shows the wave just after the time of first inundation and Fig. 14(d) shows the wave at the approximate time of maximum inundation at  $t = 2400$  s. Cross sections through the sea surface along  $y = 0$  are shown in Figs 15(a)–(c). On average, the peak of the wave travels at a speed of  $148 \text{ m s}^{-1}$ , a propagation speed that falls between those for the tsunami in scenarios A and B in Section 3.

Fig. 16(a) shows the history of inundation. First inundation occurs at 2050 s. The final inundation area is  $27 \text{ km}^2$  and the maximum run-up length is 492 m after  $t = 2410$  s. These characteristics are an order of magnitude larger than in Scenarios A and B, highlighting the impact of large and slow slip on a curved fault even during a fully buried, low stress drop event. Maximum run-up is increased in particular.

#### 4.2.1 Comparison to tsunami from a time-independent source

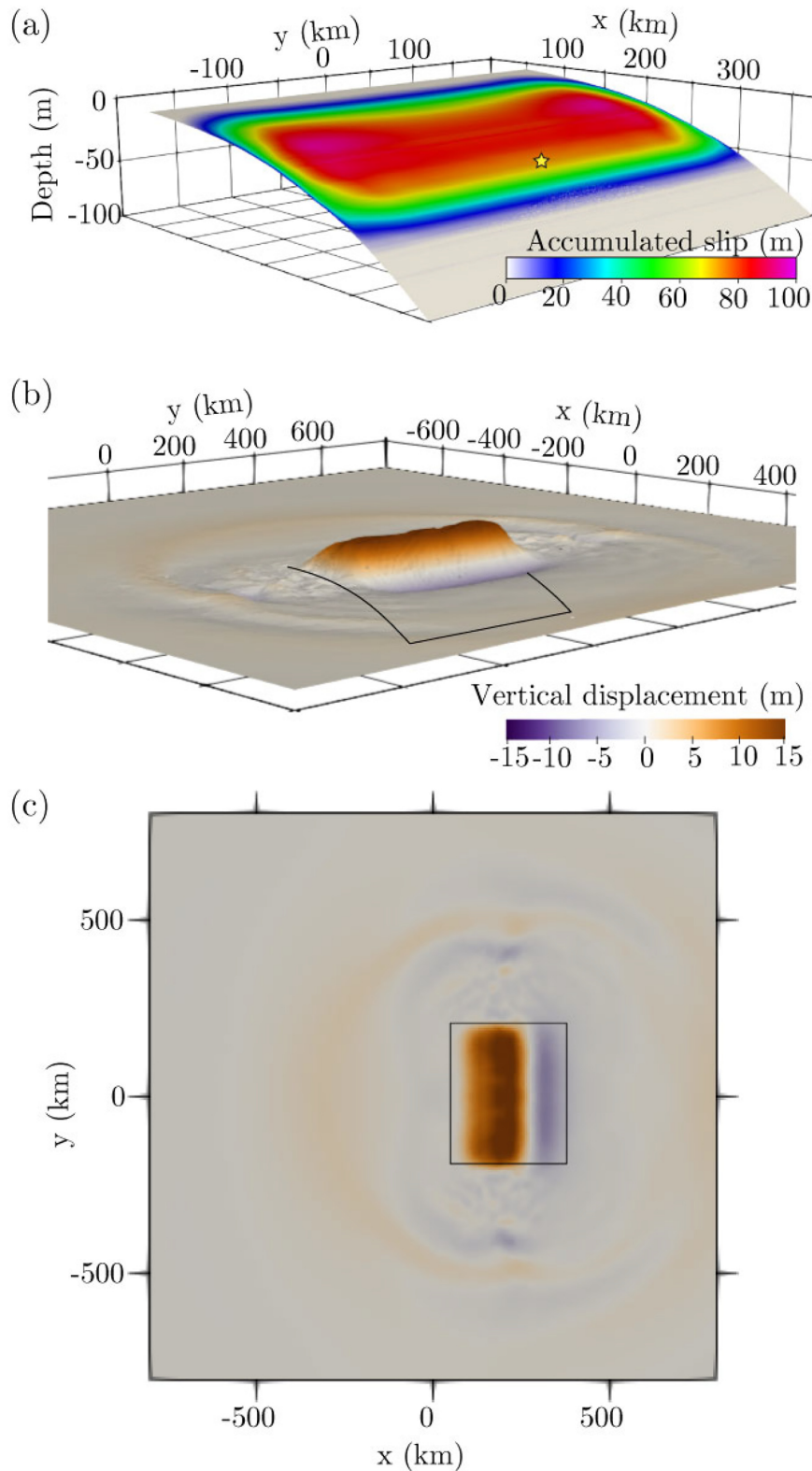
We now model the tsunami using only the time-independent filtered displacements from the end of the earthquake model, instead of the time-dependent filtered displacements from throughout the dynamic earthquake rupture in Scenario C. The tsunami from this time-independent source arrives at the coast 200 s earlier than the tsunami from the time-dependent source, so we shift the simulation results by 200 s to synchronize the scenarios to the time when the coast is first inundated. The maximum time-independent seafloor uplift is lower than the maximum uplift during the entire earthquake, though the mean displacement values for both cases are much closer (Table 1).

Fig. 16(b) shows the inundation region for the tsunami from the time-independent source and Fig. 16(c) compares this to the original tsunami in Fig. 16(a). Using a time-independent source overpredicts the run-up distance, as for the tsunami sourced by the surface breaching rupture in Scenario B, but produces a narrower inundation corridor at all distances from the coast. While the time-independent source generally delays inundation, it advances the time of first inundation near  $y = -200$  km and  $y = 200$  km. It also advances inundation at the points most distant from the coast. In general, the temporal characteristics are more distorted by the change to a time-independent source than the spatial characteristics, as may be expected.

Figs 17(a) and (b) compare the wave profiles from the time-independent and time-dependent sources at  $t = 420$  s. Along  $y = 0$ , the wave pattern is similar for both sources, but the time-independent source produces a 1.1 m higher peak and this peak is advanced ahead of that in the original source (Fig. 17a). At  $y = 150$ , the time-independent source produces a wave peak that is 1.3 m lower than for the time-dependent source, but the two wave peaks are in similar locations (Fig. 17b). Figs 17(c) and (d) compare the waves for the static and dynamic cases in time at the coast ( $x = 540$  km). At  $y = 0$ , the time-independent source again over predicts the peak wave height (Fig. 17c), but the peak from the time-independent source is again slightly underpredicted at  $y = 150$  (Fig. 17d).

#### 4.3 Conclusion

In comparison to the two scenarios in Section 3, the average dynamic stress drop and rupture velocity for this subduction-initialized



**Figure 12.** Results from the subduction-initialized dynamic earthquake rupture in Scenario C at  $t = 230$  s: (a) accumulated slip on the fault, (b) oblique view of the vertical surface displacements and (c) map view of the vertical surface displacements. Black lines in (b) and (c) outline the fault.

earthquake are lower, but fault slip and seafloor uplift are larger. The fault does not intersect with the surface, so the rupture is blind. We find that large and slow slip on a curved fault significantly impact tsunami characteristics, particularly maximum run-up, even in a

fully buried and low stress drop event. Use of time-independent instead of time-dependent filtered displacements in the tsunami source overpredicts wave peaks at  $y = 0$ , but underpredicts peaks away from this location. This results in an underestimate of the width of the

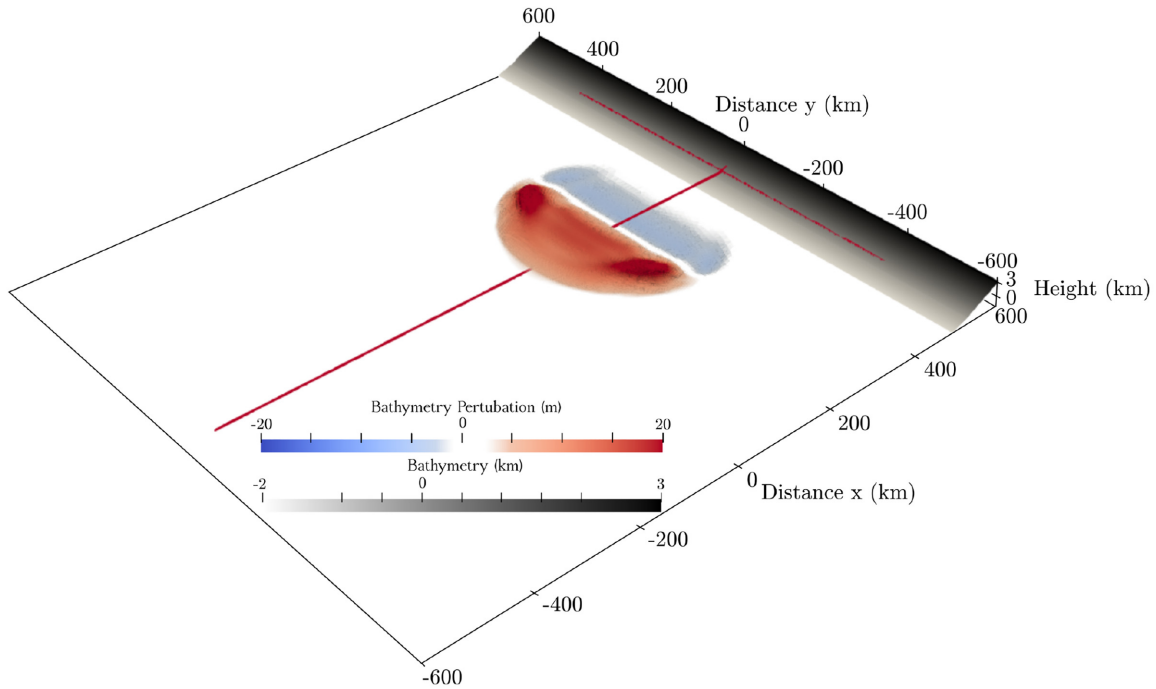


**Figure 13.** The tsunami physical model showing the bathymetric perturbation,  $\Delta b$ , at  $t = 100$  s incorporating displacements from the subduction-initialized earthquake in Scenario C. Red lines are at  $y = 0$  and at the coast at  $x = 540$  km.

inundation corridor everywhere except in the central region inland from the coast. Run-up is also overpredicted. Temporal differences include delayed arrival at the central coast, but advanced arrival along the more distant coast and at the locations farthest inland.

## 5 DISCUSSION

We here discuss selected aspects of the presented methods for linking subduction, dynamic earthquake rupture and tsunami models. We generalize on the use of time-independent versus time-dependent displacements as tsunami sources, compare the earthquakes and tsunamis in Scenarios A, B and C with real events, and contrast the tsunami-generating efficiency of the earthquakes in all three scenarios. We end with a look forward.

### 5.1 3-D dynamic earthquake model—shallow water tsunami model linking

Use of a hydrostatic shallow water tsunami model in the linked modelling chain allows for evaluation of not only tsunami generation and propagation through open water, but also inundation at the coast. In this workflow, we remove trailing seismic waves and specifically surface waves with a space–time Fourier-transform based filter. Fig. 18 shows the filtered vs. unfiltered source at  $t = 249$  s, the end of the dynamic rupture model in the subduction-initialized earthquake (Scenario C). Note that the general uplift is kept unchanged, while the waves characterized by high ratios of frequency to wavelength (fast propagating waves/short wavelengths) surrounding the uplift area are effectively damped. We note that Saito *et al.* (2019) use a low-pass filter, which does not completely eliminate the seismic waves from the tsunami signal near the source. Although we leave a full computational analysis to future work, we additionally find that the discretized shallow water solver also acts as a filter, since the fast wave creates a short impulse of momentum

that decays immediately after the wave has passed, leaving the water column basically untouched.

The linked modelling approach permits study of tsunami sensitivity to source time dependence in scenario cases, complementing heuristic findings (e.g. Davies 2019). We compare tsunami sourced by the time-dependent, filtered bathymetry perturbation with those sourced by the perturbation considering the time-independent displacements at the end of each earthquake scenario. We find, as may be expected, that temporal differences are larger than spatial differences.

In all three scenarios, use of a time-independent source results in more constant arrival times at the coast; the coast near the hypocentre is inundated later and the more distant coast is inundated earlier than for the tsunami with the time-dependent source. This behaviour is consistent with a simulation of the 2004 Indian Ocean tsunami (Poisson *et al.* 2011), where earlier wave arrivals result from a time-independent tsunami source.

Use of a time-independent source in Scenarios B and C (with surface-breaching and subduction-initialized earthquakes, respectively) overpredicts run-up. In Scenario C, the width of the inundation corridor is underpredicted at all distances from the coast. This is not the case for Scenarios A or B, however, where the width of the inundation corridor remains relatively unchanged. This effect in Scenario C may be related to overprediction of the central wave peak (at  $y = 0$ ) and underprediction of the wave peaks away from here.

We see that the highest seafloor displacements over the entire duration of the earthquake do not control the tsunami heights during propagation to first order, but may control the width of the inundation corridor inland from the coast. This is seen in Scenarios A and B, which have seafloor displacements that differ by 35 per cent, but exhibit a decreasing difference in peak wave height during propagation. The narrower inland inundation corridor for the blind rupture reflects its lower maximum seafloor displacements.

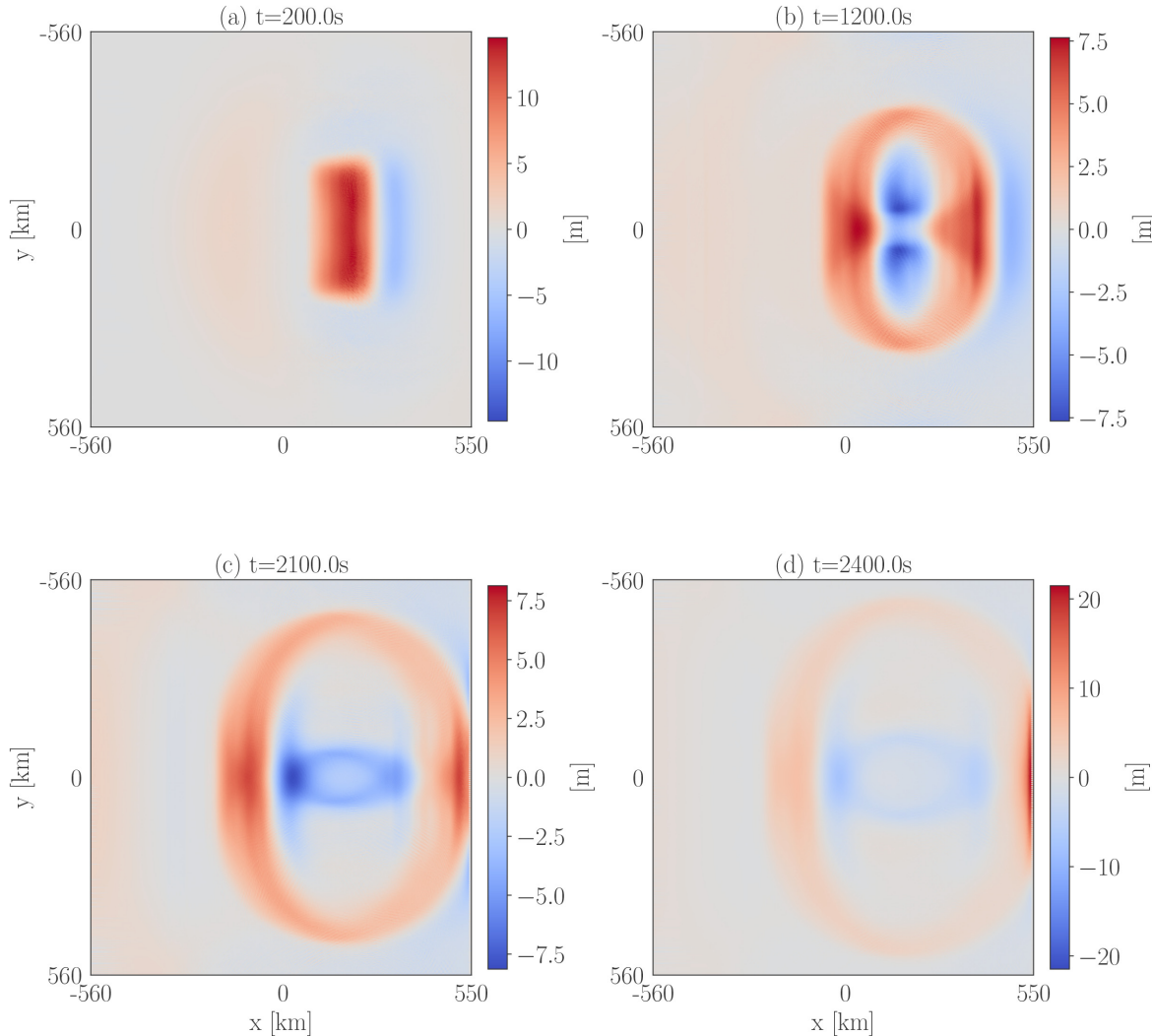


**Figure 14.** Sea surface height (ssh) from the tsunami sourced by the subduction-initialized earthquake in Scenario C at (a) the end of the earthquake, (b) after evolving for 1000 s, (c) the approximate time of first inundation and (d) the approximate time of maximum inundation.

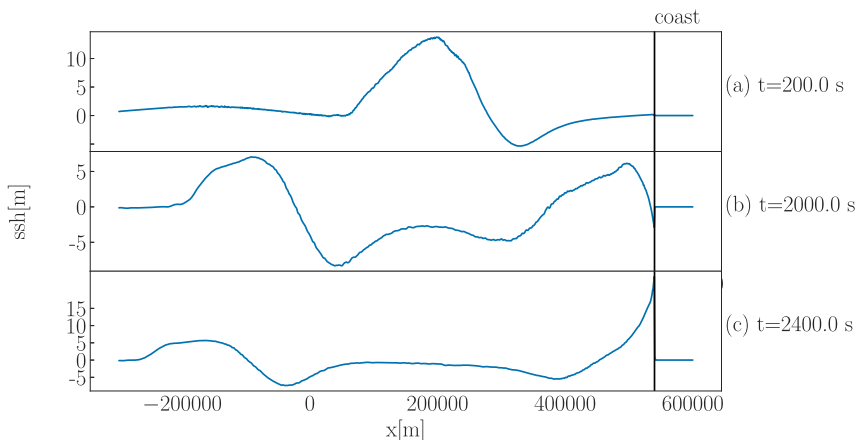


**Figure 15.** Sea surface height (ssh) from the tsunami sourced by the subduction-initialized earthquake in Scenario C along  $y = 0$  at (a) the end of the earthquake, (b) the approximate time of first inundation and (c) the approximate time of maximum inundation.

This is also seen when comparing tsunamis from time-dependent and time-independent sources. In all scenarios, the highest seafloor displacements are consistently higher than the maximum displacements from the end of the earthquake that are used in the

time-independent source (by up to an order of magnitude in case of Scenario C, Table 1). However, the peak wave heights from the time-dependent and time-independent sources are similar. This suggests that it is the more comparable average displacements that

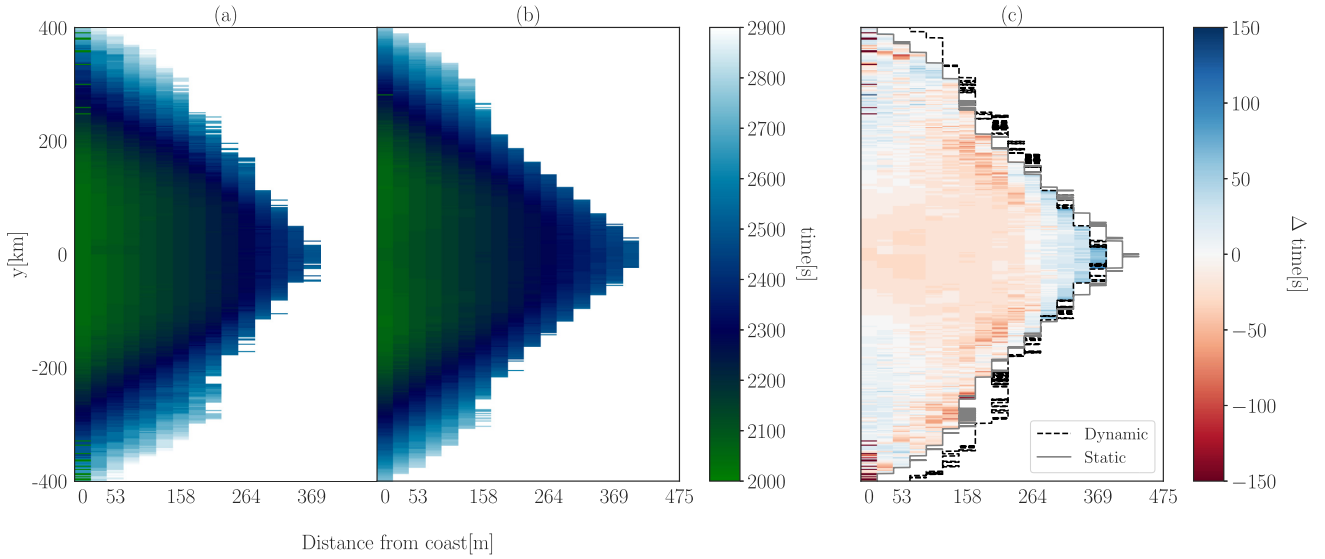


**Figure 16.** Inundation in space and time for the tsunami in Scenario C from the subduction-initialized earthquake. Coast is at  $x = 540$  km. The first time the coast is inundated by the tsunami from (a) the time-dependent source, (b) the time-independent source and (c) the difference (time-dependent minus time-independent). Negative values indicate that tsunami from the time-independent source arrives later.

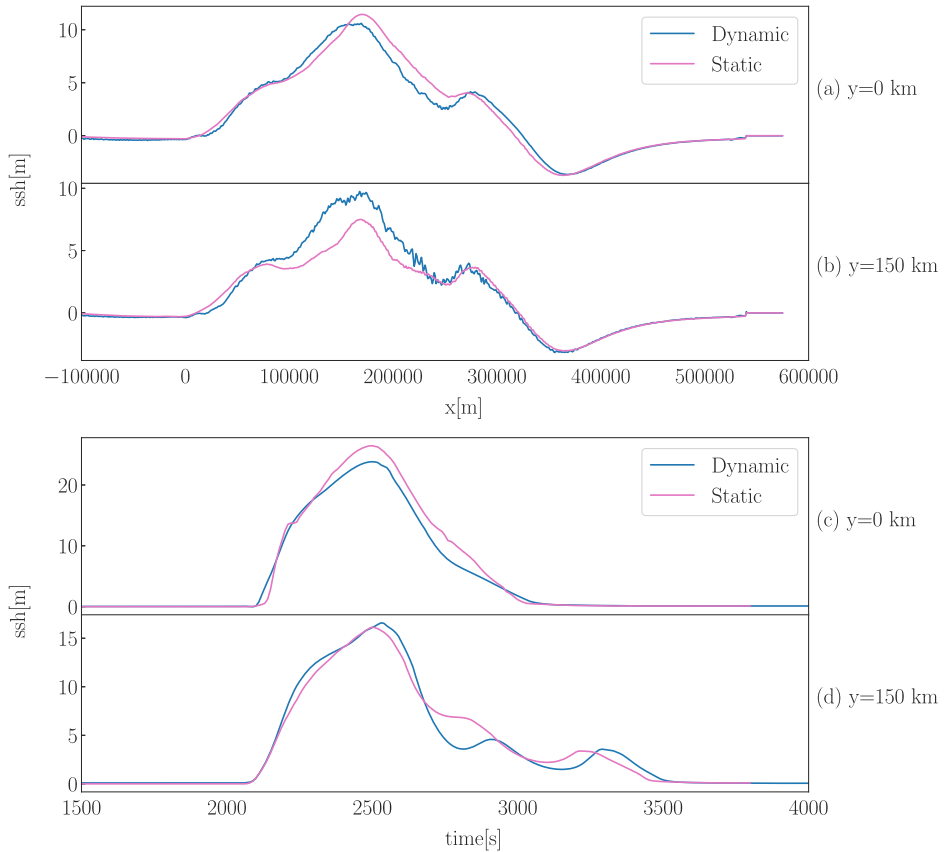


**Figure 17.** Comparison of sea surface height (ssh) from the tsunami from the time-dependent source and the time-independent sources in Scenario C at  $t = 420$  s along cross sections near (a)  $y = 0$  km and (b)  $y = 150$  km. Comparison of sea surface height (ssh) over time at points on the coast near (c)  $x = 540$  km and  $y = 0$  km and (d)  $x = 540$  km and  $y = 150$  km.

control tsunami wave heights, because they control the volume of water displaced.

In Scenario C, the inundation area of the tsunami from the time-independent source is narrower than that from the time-dependent source (Fig. 16c). This is also seen when comparing

the tsunamis from the time-dependent sources from Scenario A versus Scenario B (Fig. 7c) and when comparing the tsunamis from the time-independent sources from Scenario A versus Scenario B (Fig. 7f). We attribute the narrower inundation corridors to the relatively low transient displacements during the associated

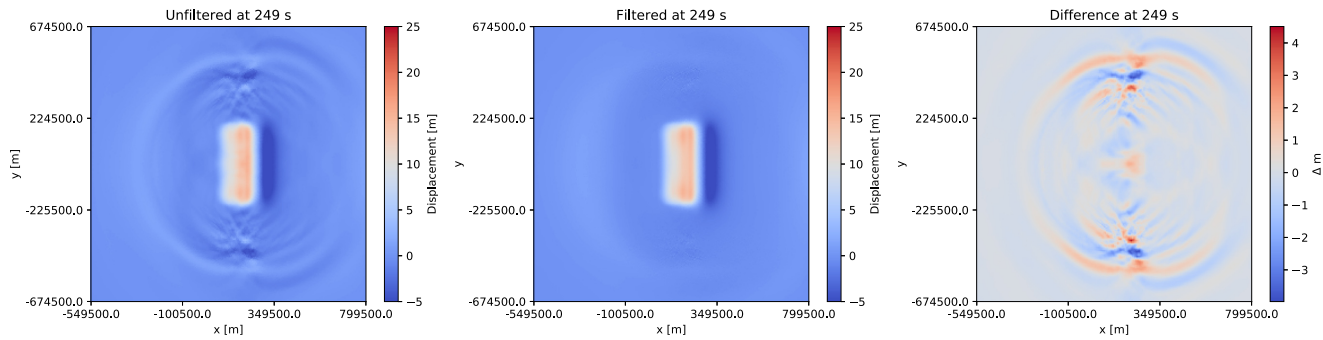


**Figure 18.** Effect of the time space Fourier filter on the the bathymetric perturbation,  $\Delta b$ , from the subduction-initialized earthquake in Scenario C at  $t = 249$  s. The filter uses (a) the raw field as input and produces (b) a filtered perturbation field from which (c) unwanted seismic surface waves and trailing seismic waves were cleaned.

earthquakes. However, this effect is not pronounced when comparing the tsunamis from the time-dependent versus time-independent sources in Scenario A (Fig. 7g) or from the time-dependent versus time-independent sources in Scenario B (Fig. 7h). These types of differences, shown here in generic models, may be challenging to distinguish from field data, for which regional and data-driven adjustment of the scenarios may be required.

## 5.2 Subduction model—3-D dynamic earthquake rupture model linking

Initializing the earthquake dynamic rupture model with a subduction model provides coherent initial conditions in the earthquake model that typically are poorly constrained. Furthermore, this ensures compatibility of those conditions, i.e., with long term subduction and seismic cycling, as shown here, as well as with splay faulting in the accretionary wedge (van Dinther *et al.* 2013b, 2014; van Zelst *et al.* 2019). This is particularly relevant in cases where splay faulting may be a major part of the tsunami source, for example in the 2004 Sumatra–Andaman earthquake and Indian Ocean tsunami (e.g. Chauhan *et al.* 2009; DeDontney & Rice 2011).

Linearly varying or constant stress with depth is often incorporated into dynamic rupture models (e.g. Kozdon & Dunham 2013; Ramos & Huang 2019; Ulrich *et al.* 2019b) alongside constant frictional parameters and homogeneous material properties. Initial conditions for the earthquake scenarios in Section 3 reflect these assumptions, including a homogeneous material, linearly increasing normal and shear tractions, a planar fault, and constant frictional parameters. The fault experiences a linearly increasing static strength with depth (Fig. 2). However, what the initial conditions in the subduction-initialized earthquake in Section 4 reveal are shear traction and static friction depth profiles that vary with both depth and material, with the most obvious change from sediments to oceanic crust at approximately 28 km depth (Fig. 10). There is also variability in the static and dynamic friction coefficients with depth. This is a far greater (and continuous) range of values than are provided by laboratory measurements on a select number of samples. It also provides context for different results that may emerge from field studies of a single subduction zone.

Because we assume that the fault, material properties and all linked on-fault conditions are constant in the third dimension not provided by the 2-D subduction model, this approach still simplifies conditions relative to nature. Nonetheless, the heterogeneity directly influences the earthquake dynamics and therefore the tsunami source. For example, although the maximum fault strength

is similar in all three scenarios presented here, the heterogeneous initial conditions for the subduction-initialized earthquake result in larger fault slip, but lower average dynamic stress drop and rupture velocity. This may correspond to natural megathrust behaviour. In addition, we observe that seismic waves traveling through complex materials around the fault (as opposed to a homogeneous material) influence earthquake dynamics, affecting rupture style and shallow slip accumulation.

These linking methods also provide avenues for investigating earthquake nucleation. We here run the entire seismic cycling phase of the subduction model and then select one slip event from the series of quasi-periodic events. We then identify the beginning of this event as the time step when two adjacent points are at failure due to local exceeding of the failure criterion. In 2-D coupling by van Zelst *et al.* (2019), these two points constitute the nucleation line on a 1-D fault that lead to a dynamic earthquake rupture. Along a 3-D fault, we must laterally restrict this location and do so by creating a 2-D nucleation patch centred on these points at failure. Assigning a lower effective dynamic friction coefficient inside than outside of this patch, with both values taken directly from the subduction model, sustained dynamic earthquake rupture is initiated. Future work may investigate the sensitivity of nucleation to patch radius, patch shape or other characteristics. Also, future exploration of the relationship between slip initiation in the earthquake model and strain rate or slip rate in the subduction model may provide insight into the nature of slip nucleation itself.

## 5.3 Realistic scenarios?

Here we compare the linked scenarios against observed events, evaluating not only if a reasonable and/or realistic modelled tsunami is produced from a particular earthquake source, but also if that modelled earthquake is itself a reasonable/realistic event. We discuss the effects of slip-to-the-trench, and compare the tsunami-generating efficiency of the earthquakes in all three scenarios.

### 5.3.1 Blind versus surface-breaching ruptures (Scenarios A and B)

Prior to the 2011 Tohoku earthquake, the compliance and velocity strengthening behaviour of shallow subduction zone materials was thought to prohibit fault slip near the trench. Most finite fault inversions restricted shallow slip, as for example slip inversions for the 2004 Sumatra–Andaman earthquake (Shearer & Burgmann 2010).

In this case, the large Indian Ocean tsunami originally was attributed to splay faulting, launching both field and modelling investigations (e.g. Chauhan *et al.* 2009; DeDontney & Rice 2011). However, seafloor observations of the 2011 Tohoku earthquake changed this view. In the case of the 2004 Sumatra-Andaman earthquake, recent investigations suggest that lithification of shallow sediments could permit slip at near or at the trench (Gulick *et al.* 2011; Hüpers *et al.* 2017).

These considerations motivated the two tsunami sources in Section 3. We expected that the blind and surface-breaching ruptures in scenarios A and B would produce distinctly different tsunamis and the surface-breaching rupture would inundate a larger area than the blind rupture (Fig. 7c). Inundation area is 15 per cent larger for the surface-breaching rupture. However, despite differences in the earthquake slip distributions and maximum slip values, the difference in peak wave height at the coast is small, and coastal inundation extent and run-up are the same in both scenarios. We note that the seafloor displacements in both scenarios differ less than the slip, partially explaining this contrast.

To better understand this, we calculate the efficiency of the Scenario A and Scenario B earthquakes in generating the resulting tsunamis as  $\epsilon$  following Lotto *et al.* (2017a):

$$\epsilon = h_{\max} / \langle s \rangle, \quad (6)$$

where  $h_{\max}$  is the maximum wave height near the source (here, taken at  $t = 56$  s) and  $\langle s \rangle$  is mean slip. In Scenario A,  $\epsilon_A = 0.7$ . In Scenario B,  $\epsilon_B = 0.5$ . Thus, although Scenario B includes shallow slip and larger maximum seafloor displacements that contribute to a higher initial wave height, the source is less efficient at producing a tsunami than is the source in Scenario A. Such trade-off may explain why the differences between the two tsunami events are limited. We also note that the highly complex Scenario C earthquake matches the efficiency of Scenario A at  $\epsilon_C = 0.7$  (see Section 5.3.2). The relative loss of efficiency in Scenario B may be due to inefficiency of shallow slip in this surface-breaching earthquake.

The presented 3-D scenarios lead to tsunami efficiencies that are considerably higher than for those from the 2-D models in Lotto *et al.* (2017a). The tsunami potential energy as defined by Melgar *et al.* (2019) may be useful to further compare scenarios, as it accounts for the combined effects of various source properties on the sea surface dislocation. However, it is yet a time-independent parameter.

Extending dynamic rupture conditions in linked 3-D earthquake-tsunami modelling beyond the slip-weakening on-fault behaviour and elastic off-fault deformation also will deepen understanding of how near-surface earthquake dynamics control tsunami behaviour and  $\epsilon$ . For example, Ma (2012) and Ma & Nie (2019) highlight the importance of plastic yielding in modelling uplift landward of the trench for the 2011 Tohoku earthquake. In a detailed study of the role of accretionary prisms in 2-D coupled earthquake-tsunami models, Lotto *et al.* (2017a) find that prisms that are more compliant than the surrounding material tend to slow earthquake rupture speeds, increase slip, and induce larger tsunamis. Here, the relatively low strength of the shallow fault in Scenario B permits surface-breaching rupture, but leads to localized supershear rupture velocities. Incorporating off-fault deformation should allow for modelling slip at the trench at locally slow rupture velocity.

We next compare the modelled Scenarios A and B with real earthquakes and tsunamis. Based on their magnitudes ( $M_w$  8.5–8.6), fault area (125 km by 200 km), and slip distributions, the

two earthquakes scenarios are comparable to tsunami-generating subduction zone events such as the  $M_w$  8.5 Bengkulu earthquake that occurred off the southwestern coast of Sumatra in 2007 (Gusman *et al.* 2010; Seno 2014) and the  $M_w$  8.5 South Peru earthquake that occurred in 2001 (Pritchard *et al.* 2007; Seno 2014). The Bengkulu earthquake had slip restricted to below 10 km depth, with most slip occurring at 16–40 km depth and reaching a maximum of 6–7 m (Gusman *et al.* 2010). The slip distribution and maximum slip in the Scenario A earthquake are consistent with this event. In the 2001 South Peru earthquake, high slip may have occurred at shallow depths, though whether or not slip occurred at the trench is inconclusive (Pritchard *et al.* 2007). The slip distribution in the Scenario B earthquake is similar to this, though slip in this scenario reaches a maximum of approximately 10 m at the trench, versus the 6 m maximum slip in the South Peru event (Pritchard *et al.* 2007).

The blind Bengkulu earthquake rupture produced a tsunami that was recorded at several tide gauges in the Indian Ocean, with a maximum peak-to-trough wave height of 2.3 m at Padang (USGS accessed 2020-07-03). The potentially surface-breaching rupture in the 2001 South Peru earthquake produced a tsunami with wave heights of 1.0–2.5 m at three different tide stations (USGS accessed 2019-07-22). These maximum recorded wave heights are lower than the peak wave heights at the coast for the modelled blind rupture in Scenario A and surface-breaching rupture in Scenario B of 3.4 and 3.8 m, respectively (Table 2). However, the difference between the observed waves produced by the (potentially) surface-rupturing and blind earthquakes are similar for the observed and modelled events, which may motivate future studies accounting for fault slip in the South Peru earthquake indeed reaching the surface.

Using purely tsunami based observations and linked models, for example of historical megathrust events, distinguishing between possible blind or surface rupturing earthquakes may be feasible. Satellite data capturing wave heights in the ocean have resolutions on the order of cm (Hayashi 2008) and data used to determine inundation areas have resolutions on the order of m to tens of m (Koshimura *et al.* 2020), both of which are at the scale of the modelled differences between tsunamis in Scenarios A and B. Future modelling can also strive to quantify differences of the same orders of magnitude attributed to other dynamic earthquake and tsunami characteristics.

### 5.3.2 Subduction-initialized earthquake and tsunami (Scenario C)

The subduction-initialized earthquake in Section 4 is a  $M_w$  9.0 event. The efficiency of this earthquake in generating the modelled tsunami is calculated using eq. (6). With  $h_{\max}$  is taken near the source at  $t = 100$  s,  $\epsilon_C = 0.7$ , which matches the efficiency of the blind earthquake rupture in Scenario A.

Scenario C's magnitude and the model fault dimensions are similar to those for the 2011  $M_w$  9.0 Tohoku megathrust earthquake. The rupture speed in this scenario varies along the fault, but averages  $2.1 \text{ km s}^{-1}$ , somewhat similar to the  $2.5 \text{ km s}^{-1}$  mean rupture speed estimated for the Tohoku earthquake by Ammon *et al.* (2011) after the first 80 s of the rupture. The average and maximum accumulated slip for the modelled earthquake (42.2 and 95.6 m, respectively) are at or above the upper limit of what is observed in smoothed slip inversions for the 2011 Tohoku earthquake (Sun *et al.* 2017). In addition, the modelled maximum vertical seafloor displacement is 28.1 m and not at the trench, while maximum values from the Tohoku earthquake are estimated to be  $\sim 10$  m at the trench

(Fujiwara *et al.* 2011; Sun *et al.* 2017). Direct comparison between the modelled tsunami results and the Tohoku tsunami observations is hampered by the complex interplay of bathymetry, sea surface height, and wave travel time, but we expect higher slip in the scenario than observed for this event to also be reflected in a larger tsunami in the scenario than observed. Indeed, the modelled peak-to-trough height at the coast is 24 m, compared to observations following the Tohoku rupture of 6.8 m at Iwate Kamaishi-oki and 6 m at several other locations (Japan Meteorological Agency 2019).

To modify Scenario C to capture, for example, the Tohoku earthquake and tsunami or other past or future megathrust earthquake scenarios, lower modelled slip could be achieved with different model linking choices, such as a higher Poisson's assigned ratio, or by adding fault complexity in the third dimension. For instance, choosing a larger  $\nu$ , keeping all other parameters constant, results in less fault slip during an earthquake modelled in 2-D (van Zelst *et al.* 2019). Alternatively, adjusting the subduction model itself to be region specific, for example to the Japan trench, would provide more direct constraints on fault geometry and other initial conditions.

#### 5.4 Looking forward

One main advantage of linked earthquake-tsunami modelling is that the model complexity can be readily increased or decreased, depending on the hypothesis being tested. For example, realistic representations of complex topography and bathymetry are permissible in both the earthquake and tsunami computational models, which may be critical not only for inundation modelling, but also for modelling tsunami genesis and propagation in deep water (e.g. Salaree & Okal 2020).

Similarly, we here restrict the off-fault constitutive behaviour of the earthquake physical models to purely elastic and use a linear slip weakening friction law on-fault. However, recent 3-D earthquake-tsunami models of the 2004 Sumatra earthquake reveal the sensitive trade-off between shallow fault slip and off-fault elastoplastic deformation in controlling the tsunami height (Ulrich *et al.* 2020). Future linked modelling can help to elucidate how these aspects of earthquake dynamics influence tsunami behaviour by readily switching to, for example, alternative friction laws such as rate-and-state, elastoplastic off-fault and wedge behaviour or thermal pressurization of pore fluids.

Tsunami generation from landslides is simulated well by established software (e.g. Clawpack, Mandli *et al.* 2016), but landslide sources are not incorporated into the presented modelling chain. However, this chain can provide a way to test the importance of earthquake dynamics in the tsunami source (e.g. Ulrich *et al.* 2019b) and trade-offs with other sources. For example, several recent modelling efforts related to the 2018 Sulawesi earthquake and tsunami, combining displacements from earthquakes and landsliding, underscore the importance of dual source mechanisms (e.g. Heidarzadeh *et al.* 2019; Aránguiz *et al.* 2020).

When initializing the earthquake model from a subduction model, we must honor the plane-strain conditions of the 2-D subduction model while mapping the stress field into the 3-D earthquake model. This most likely does not reflect conditions *in situ*. Ideally, one would incorporate the dynamic earthquake rupture into seismic cycling in the subduction model. Methodological advances may enable linking with a 3-D subduction model and working toward this two-way coupling between earthquake dynamics and long term behaviour.

Coupled feedback mechanisms beyond one-way linking from earthquake to tsunami also may be analysed in future work. For example, the two-way interaction of the water column and the solid Earth may be considered. As the feedback of pressure differences in the water column to the solid bottom is small in the models presented here (1 m of water wave height corresponds to approximately 0.1 bar or 10 kPa), the assumption of a rigid crust may not affect rupture evolution. However, assuming a rigid crust has been shown to influence the tsunami in the far-field and lead to earlier arrival times than observed (Watada *et al.* 2014). Interest in how acoustic waves affect tsunami signals is growing with the expansion of near-source ocean-bottom sensors (e.g. Maeda *et al.* 2011; Saito *et al.* 2019; Saito & Kubota 2019). Saito *et al.* (2019) find that they do affect the near-source tsunami signal, but have little influence on propagation beyond the time it takes for the waves to exit the region of the slower tsunami. Full 3-D coupling of the seismic, acoustic and gravity seafloor and water column displacements using the same computational tools is underway (Abrahams *et al.* 2019; Krenz *et al.* 2019), but is computationally challenging.

The scenarios presented in this paper are accompanied by detailed input files and model information (see Appendix A). This provides sufficient detail for other modellers to run all or parts of these scenarios in their linked model setup and compare their results to these. In future work, these applications may also be useful for community-wide comparison of dynamic earthquake-tsunami modelling approaches and alternative linking methods.

## 6 CONCLUSIONS

Surprises with devastating consequences in past earthquake-tsunami sequences motivate a better understanding of the physical connections between subduction, earthquake dynamics and tsunami from genesis to inundation. Modelling approaches bridging physical parameters and processes across these temporal and spatial scales are suited to help advance such research. We here use 3-D dynamic rupture models as tsunami sources by building a virtual laboratory using open-source earthquake and tsunami computational models. We present three scenario applications to demonstrate the flexibility and capabilities of this linked modelling.

These methods are well-suited for hypothesis testing, such as isolating the influence of a single parameter on earthquake and tsunami behaviour. In scenarios A and B, we compare tsunamis from a blind rupture and a surface-breaching rupture due to differing fault strength near the surface. The surface-breaching rupture does inundate a wider area inland from the coast, but we find that slip to the trench does not cause differences in inundation shape, change run-up or alter the length of coast impacted. This similarity may result from trade-off between the blind rupture's higher tsunami-generating efficiency and the surface-breaching rupture's larger shallow slip, which leads to higher seafloor displacements and a larger displaced volume of water.

We use a subduction model to initialize the earthquake model in Scenario C. This approach provides reasonable earthquake initial conditions that typically are poorly constrained by data, but which exert first-order control over rupture behaviour. Setting up the earthquake model in this way ensures physical consistency of the tsunami source with characteristics of both the subduction channel and the earthquake kinematics and dynamics. The resulting earthquake model includes a curved fault geometry and heterogeneous

material properties and stress field, and the frictional parameters along the fault vary with depth. Due to these highly heterogeneous on- and off-fault conditions, the earthquake in this scenario has larger slip, but lower stress drop and slower rupture speed relative to the ruptures in scenarios A and B.

Future applications of these linked modelling methods can take advantage of the flexible adjustment of tsunami and earthquake model complexity. Direct studies of how subduction characteristics, earthquake initial conditions and earthquake dynamics govern tsunami behaviour can help understand hazard in a given subduction zone. Such modelling may be specifically useful to constrain earthquake rupture and tsunami generation, propagation and inundation in complex megathrust systems, producing tsunami sources accounting for, for example, the effects of the slip to the trench, dynamic interaction between different fault segments (including splay faults) and off-fault coseismic deformation.

## ACKNOWLEDGEMENTS

This effort has and continues to require intense cross-disciplinary collaboration and we want to acknowledge the strong team effort that has made it possible. In addition to the authors, a wide group has contributed to this effort. First, we would like to thank the Volkswagen Foundation (VolkswagenStiftung) for extended funding and excellent support of the ASCETE and ASCETE II projects ([www.ascete.de](http://www.ascete.de)). Second, we want to recognize the following researchers that have contributed directly to this project over its years in development: N. Beisiegel, A. Breuer, L. Dalguer, A. Fichtner, P. Galvez, H. Igel, A. Jeschke, M. Käser, O. Meister, C. Pelties, K. Rahnema, S. Rettenberger and S. Wollherr.

Finally, participants in the 1st and 2nd ASCETE Workshops on Coupling Earthquakes and Tsunamis held in Sudelfeld Bayrischzell, Germany provided motivation for the development of these test cases and feedback on their design. We look forward to continuing discussions with the earthquake and tsunami modelling communities. We also would like to recognize the exceptional editorship by Editors Gabi Laske and Duncan Agnew, and to thank the reviewers, Joao Duarte, Brittany Erickson, Duncan Agnew and one anonymous reviewer, for their collegial and constructive reviews.

Computing resources were provided by the Institute of Geophysics of LMU Munich (Oeser *et al.* 2006), the Leibniz Supercomputing Centre (LRZ, projects no. h019z, pr63qo and pr45fi on SuperMUC), the Center for Earth System Research and Sustainability (CEN) at University of Hamburg, and the Swiss National Supercomputing Center (project no. s741).

E.H.M., T.U. and A.-A.G. acknowledge additional support by the German Research Foundation (DFG, projects no. GA 2465/2-1, GA 2465/3-1), by BaCaTec (project no. A4) and BayLat, by KONWIHR – the Bavarian Competence Network for Technical and Scientific High Performance Computing (project NewWave), by KAUST-CRG (GAST, grant no. ORS-2016-CRG5-3027 and FRAGEN, grant no. ORS-2017-CRG6 3389.02), by the European Union’s Horizon 2020 research and innovation program (ExaHyPE, grant no. 671698, ChEESE, grant no. 823844 and TEAR, grant no. 852992).

We would like to thank the editorial team at GJI under Editor Prof Gabi Laske for handling this cross-disciplinary manuscript in such a careful and constructive way. We also appreciate the collegial reviews from Joao Duarte, Brittany Erickson, Duncan Agnew and one anonymous reviewer.

## DATA AVAILABILITY STATEMENT

We provide all necessary information and data sets required to reproduce the results presented in this work at <https://tinyurl.com/yxn6zrqc>. The archive includes all required configuration files, compilation parameters and input data.

## REFERENCES

- Aagaard, B.T., Anderson, G. & Hudnut, K.W., 2004. Dynamic rupture modeling of the transition from thrust to strike-slip motion in the 2002 Denali fault earthquake, alaska, *Bull. seism. Soc. Am.*, **94**(6B), S190–S201.
- Abrahams, L.S., Krenz, L., Dunham, E.M. & Gabriel, A.-A., 2019. Verification of a 3D fully-coupled earthquake and tsunami model, in *AGUFM*, pp. NH43F-1000, AGU.
- Allgeyer, S. & Cummins, P., 2014. Numerical tsunami simulation including elastic loading and seawater density stratification, *Geophys. Res. Lett.*, **41**(7), 2368–2375.
- Amlani, F. *et al.*, 2019. Supershear tsunamis and insights from the  $m_w$  7.5 Palu earthquake, arXiv:1910.14547 [physics.geo-ph].
- Ammon, C.J., Lay, T., Kanamori, H. & Cleveland, M., 2011. A rupture model of the 2011 off the Pacific coast of Tohoku Earthquake, *Earth, Planets Space*, **63**(7), 693–696.
- Ando, R. & Kaneko, Y., 2018. Dynamic rupture simulation reproduces spontaneous multifault rupture and arrest during the 2016  $M_w$  7.9 Kaikoura Earthquake, *Geophys. Res. Lett.*, **45**(23), 12 875–12 883.
- Andrews, D., 1980. A stochastic fault model: 1. Static case, *J. geophys. Res.*, **85**(B7), 3867–3877.
- Andrews, D.J., 1976. Rupture velocity of plane strain shear cracks., *J. geophys. Res.*, **81**(32), 5679–5687.
- Andrews, D.J., 2005. Rupture dynamics with energy loss outside the slip zone, *J. geophys. Res.*, **110**(B1), B01307.
- Aochi, H. & Fukuyama, E., 2002. Three-dimensional nonplanar simulation of the 1992 Landers earthquake, *J. geophys. Res.*, **107**(B2), ESE–4.
- Aránguiz, R. *et al.*, 2020. The 2018 Sulawesi tsunami in Palu city as a result of several landslides and coseismic tsunamis, *Coastal Eng. J.*, 1–15, doi:10.1080/21664250.2020.1780719.
- Babeyko, A.Y., Hoechner, A. & Sobolev, S.V., 2010. Source modeling and inversion with near real-time GPS: a GITEWS perspective for Indonesia, *Nat. Hazards Earth Syst. Sci.*, **10**(7), 1617–1627.
- Bai, K. & Ampuero, J.-P., 2017. Effect of seismogenic depth and background stress on physical limits of earthquake rupture across fault step overs, *J. geophys. Res.*, **122**(12), 10–280.
- Behrens, J. & Dias, F., 2015. New computational methods in tsunami science, *Phil. Trans. R. Soc., A*, **373**(2053), 20140382.
- Berger, M.J., George, D.L., LeVeque, R.J. & Mandli, K.T., 2011. The GeoClaw software for depth-averaged flows with adaptive refinement, *Adv. Water Resour.*, **34**(9), 1195–1206.
- Bizzarri, A. & Cocco, M., 2006. A thermal pressurization model for the spontaneous dynamic rupture propagation on a three-dimensional fault: 1. Methodological approach, *J. geophys. Res.*, **111**(B5), doi:10.1029/2005JB003862.
- Bleiter, Q., Sladen, A., Jiang, J. & Simons, M., 2016. A Bayesian source model for the 2004 great Sumatra-Andaman earthquake, *J. geophys. Res.*, **121**(7), 5116–5135.
- Breuer, A., Heinecke, A., Rettenberger, S., Bader, M., Gabriel, A.-A. & Pelties, C., 2014. Sustained petascale performance of seismic simulations with SeisSol on SuperMUC, in *Supercomputing. ISC 2014. Lecture Notes in Computer Science*, Vol. 8488, pp. 1–18, eds Kunkel, J.M., Ludwig, T. & Meuer, H.W., Springer.
- Breuer, A., Heinecke, A. & Bader, M., 2016. Petascale local time stepping for the ADER-DG finite element method, in *Proceedings of the 2016 IEEE International Parallel & Distributed Processing Symposium*, pp. 854–863.
- Brizzi, S., van Zelst, I., Funiciello, F., Corbi, F. & van Dinther, Y., 2020. How sediment thickness influences subduction dynamics and seismicity, *J. geophys. Res.*, **125**(8), doi:10.1029/2019JB018964.

- Chauhan, A.P.S. et al., 2009. Seismic imaging of forearc backthrusts at northern Sumatra subduction zone, *J. geophys. Int.*, **179** (3), 1772–1780
- Cockburn, B. & Shu, C.-W., 1998. The Runge-Kutta discontinuous Galerkin method for conservation laws V: multidimensional systems, *J. Comput. Phys.*, **141**(2), 199–224.
- Cramer, F. et al., 2012. A comparison of numerical surface topography calculations in geodynamic modelling: an evaluation of the ‘sticky air’ method, *J. geophys. Int.*, **189**(1), 38–54.
- D’Acquisto, M., Dal Zilio, L., Molinari, I., Kissling, E., Gerya, T. & van Dinther, Y., 2020. Tectonics and seismicity in the northern Apennines driven by slab retreat and lithospheric delamination, *Tectonophysics*, **789**, 228481.
- Dal Zilio, L., van Dinther, Y., Gerya, T. & Avouac, J.-P., 2019. Bimodal seismicity in the Himalaya controlled by fault friction and geometry, *Nat. Commun.*, **10**(48), doi:10.1038/s41467-018-07874-8.
- Davies, G., 2019. Tsunami variability from uncalibrated stochastic earthquake models: tests against deep ocean observations 2006–2016, *J. geophys. Int.*, **218**(3), 1939–1960.
- Day, S.M., Dalguer, L.A., Lapusta, N. & Liu, Y., 2005. Comparison of finite difference and boundary integral solutions to three-dimensional spontaneous rupture, *J. geophys. Res.*, **110**(B12307), doi:10.1029/2005JB003813.
- De La Puente, J., Ampuero, J.P. & Käser, M., 2009. Dynamic rupture modeling on unstructured meshes using a discontinuous Galerkin method, *J. geophys. Res.*, **114**(10), 1–17.
- DeDontney, N. & Rice, J.R., 2011. Tsunami wave analysis and possibility of splay fault rupture during the 2004 Indian Ocean Earthquake, *Pure appl. Geophys.*, **169**(10), 1707–1735.
- Douilly, R., Aochi, H., Calais, E. & Freed, A.M., 2015. Three-dimensional dynamic rupture simulations across interacting faults: the  $M_w$  7.0, 2010, Haiti earthquake, *J. geophys. Res.*, **120**(2), 1108–1128.
- Dumbser, M. & Käser, M., 2006. An arbitrary high-order discontinuous Galerkin method for elastic waves on unstructured meshes - II. The three-dimensional isotropic case, *J. geophys. Int.*, **167**(1), 319–336.
- Dunham, E.M., Belanger, D., Cong, L. & Kozdon, J.E., 2011. Earthquake ruptures with strongly rate-weakening friction and off-fault plasticity. Part 1: planar faults, *Bull. seism. Soc. Am.*, **101**(5), 2296–2307.
- Erickson, B.A. et al., 2020. The community code verification exercise for simulating sequences of earthquakes and aseismic slip (SEAS), *Seismol. Res. Lett.*, **91**(2A), 874–890.
- Fujiwara, T., Kodaira, S., No, T., Kaiho, Y., Takahashi, N. & Kaneda, Y., 2011. The 2011 Tohoku-Oki earthquake: displacement reaching the trench axis, *Science*, **334**(6060), 1240.
- Gabriel, A.-A., Ampuero, J.-P., Dalguer, L.A. & Mai, P.M., 2012. The transition of dynamic rupture styles in elastic media under velocity-weakening friction, *J. geophys. Res.*, **117**(B9), doi:10.1029/2012JB009468.
- Gabriel, A.-A., Ampuero, J.-P., Dalguer, L.A. & Mai, P.M., 2013. Source properties of dynamic rupture pulses with off-fault plasticity, *J. geophys. Res.*, **118**(8), 4117–4126.
- Gabriel, A.-A., Vyas, J.C., Ulrich, T., Ampuero, J. & Mai, M.P., 2020. 3D dynamic rupture modeling with thermal pressurization, in *Poster Presentation at 2020 SCEC Annual Meeting*, Southern California Earthquake Center.
- Galis, M., Pelties, C., Kristek, J., Moczo, P., Ampuero, J.-P. & Mai, P.M., 2015. On the initiation of sustained slip-weakening ruptures by localized stresses, *J. geophys. Int.*, **200**(2), 890–909.
- Galvez, P., Ampuero, J.P., Dalguer, L.A., Somalia, S.N. & Nissen-Meyer, T., 2014. Dynamic earthquake rupture modelled with an unstructured 3-D spectral element method applied to the 2011 M9 Tohoku earthquake, *J. geophys. Int.*, **198**(2), 1222–1240.
- Geist, E. & Yoshioka, S., 1996. Source parameters controlling the generation and propagation of potential local tsunamis along the Cascadia margin, *Nat. Hazards*, **13**(2), 151–177.
- Geist, E.L. & Oglesby, D.D., 2014. *Tsunamis: Stochastic Models of Occurrence and Generation Mechanisms*, pp. 1–29, Springer.
- Gerya, T.V. & Yuen, D.A., 2007. Robust characteristics method for modelling multiphase visco-elasto-plastic thermo-mechanical problems, *Phys. Earth planet. Inter.*, **163**, 83–105.
- Geuzaine, C. & Remacle, J.-F., 2009. Gmsh: a 3-D finite element mesh generator with built-in pre- and post-processing facilities, *Int. J. Numer. Methods Eng.*, **79**(11), 1309–1331.
- Giraldo, F.X. & Warburton, T., 2008. A high-order triangular discontinuous Galerkin oceanic shallow water model, *Int. J. Numer. Methods. Fluids.*, **56**(7), 899–925.
- Goda, K., Mai, P.M., Yasuda, T. & Mori, N., 2014. Sensitivity of tsunami wave profiles and inundation simulations to earthquake slip and fault geometry for the 2011 tohoku earthquake, *Earth, Planets Space*, **66**(1), 105.
- Gorczyk, W., Willner, A.P., Gerya, T.V., Connolly, J.A. & Burg, J.-P., 2007. Physical controls of magmatic productivity at pacific-type convergent margins: numerical modelling, *Phys. Earth planet. Inter.*, **163**(1–4), 209–232.
- Gulick, S.P.S. et al., 2011. Updip rupture of the 2004 Sumatra earthquake extended by thick indurated sediments, *Nat. Geosci.*, **4**(7), 453–456.
- Gusman, A., Tanioka, Y., Kobayashi, T., Latief, H. & Pandoe, W., 2010. Slip distribution of the 2007 Bengkulu earthquake inferred from tsunami waveforms and InSAR data, *J. geophys. Res.*, **115**, doi:10.1029/2010JB007565.
- Harig, S., Chaeroni, Pranowo, W.S. & Behrens, J., 2008. Tsunami simulations on several scales: comparison of approaches with unstructured meshes and nested grids, *Ocean Dyn.*, **58**(5–6), 429–440.
- Harris, R.A. et al., 2009. The SCEC/USGS dynamic earthquake rupture code verification exercise, *Seismol. Res. Lett.*, **80**(1), 119–126.
- Harris, R.A. et al., 2018. A suite of exercises for verifying dynamic earthquake rupture codes, *Seismol. Res. Lett.*, **89**(3), 1146–1162.
- Hayashi, Y., 2008. Extracting the 2004 Indian Ocean tsunami signals from sea surface height data observed by satellite altimetry, *J. geophys. Res.*, **113**(1), 1–9.
- Heidarzadeh, M., Murotani, S., Satake, K., Takagawa, T. & Saito, T., 2017. Fault size and depth extent of the Ecuador earthquake (Mw 7.8) of 16 April 2016 from teleseismic and tsunami data, *Geophys. Res. Lett.*, **44**(5), 2211–2219.
- Heidarzadeh, M., Muhamari, A. & Wijanarto, A.B., 2019. Insights on the source of the 28 September 2018 Sulawesi Tsunami, Indonesia based on spectral analyses and numerical simulations, *Pure appl. Geophys.*, **176**(1), 25–43.
- Heinecke, A. et al., 2014. Petascale high order dynamic rupture earthquake simulations on heterogeneous supercomputers, in *International Conference for High Performance Computing, Networking, Storage and Analysis, SC*.
- Hok, S., Fukuyama, E. & Hashimoto, C., 2011. Dynamic rupture scenarios of anticipated Nankai-Tonankai earthquakes, southwest Japan, *J. geophys. Res.*, **116**(12), 1–22.
- Hüpers, A. et al., 2017. Release of mineral-bound water prior to subduction tied to shallow seismogenic slip off Sumatra, *Science*, **356**(6340), 841–844.
- Ida, Y., 1972. Cohesive force across the tip of a longitudinal-shear crack and Griffith’s specific surface energy, *J. geophys. Res.*, **77**(20), 3796–3805.
- Jamelot, A., Gailler, A., Heinrich, P., Vallage, A. & Champenois, J., 2019. Tsunami simulations of the Sulawesi Mw 7.5 event: comparison of seismic sources issued from a tsunami warning context versus post-event finite source, *Pure appl. Geophys.*, **176**(8), 3351–3376.
- Japan Meteorological Agency, 2019. Tsunami warnings/advisories, tsunami information, 1-3-4 Otemachi, Chiyoda-ku, Tokyo 100-8122, Japan.
- Ji, C., Wald, D.J. & Helmberger, D.V., 2002. Source description of the 1999 Hector Mine, California, earthquake, part I: wavelet domain inversion theory and resolution analysis, *Bull. seism. Soc. Am.*, **92**(4), 1192–1207.
- Kame, N., Rice, J.R. & Dmowska, R., 2003. Effects of prestress state and rupture velocity on dynamic fault branching, *J. geophys. Res.*, **108**(B5), doi:10.1029/2002JB002189.
- Kanamori, H., 1972. Mechanism of tsunami earthquakes, *Phys. Earth planet. Inter.*, **6**(5), 346–359.
- Kaneko, Y., Lapusta, N. & Ampuero, J.-P., 2008. Spectral element modeling of spontaneous earthquake rupture on rate and state faults: effect of velocity-strengthening friction at shallow depths, *J. geophys. Res.*, **113**(B9), doi:10.1029/2007JB005553.
- Käser, M. & Dumbser, M., 2006. An arbitrary high-order discontinuous Galerkin method for elastic waves on unstructured meshes - I. The

- two-dimensional isotropic case with external source terms, *J. geophys. Int.*, **166**(2), 855–877.
- Klinger, Y. *et al.*, 2018. Earthquake damage patterns resolve complex rupture processes, *Geophys. Res. Lett.*, **45**(19), 10 279–10 287.
- Koshimura, S., Moya, L., Mas, E. & Bai, Y., 2020. Tsunami damage detection with remote sensing: a review, *Geosciences (Switzerland)*, **10**(5), 1–28.
- Kozdon, J.E. & Dunham, E.M., 2013. Rupture to the trench: dynamic rupture simulations of the 11 March 2011 Tohoku Earthquake, *Bull. seism. Soc. Am.*, **103**(2B), 1275–1289.
- Kozdon, J.E. & Dunham, E.M., 2014. Constraining shallow slip and tsunami excitation in megathrust ruptures using seismic and ocean acoustic waves recorded on ocean-bottom sensor networks, *Earth planet. Sci. Lett.*, **396**, 56–65.
- Krenz, L., Uphoff, C., Abrahams, L.S., Gabriel, A.-A., Dunham, E.M. & Bader, M., 2019. Elastic-acoustic coupling for 3D tsunamigenic earthquake simulations with ADER-DG on unstructured tetrahedral meshes, in *AGU FM*, pp. T52C–09, AGU.
- LeVeque, R.J., George, D.L. & Berger, M.J., 2011. Tsunami modelling with adaptively refined finite volume methods, *Acta Numer.*, **20**, 211–289.
- Liang, Q. & Marche, F., 2009. Numerical resolution of well-balanced shallow water equations with complex source terms, *Adv. Water Resour.*, **32**, 873–884.
- Liu, P.L.F., Cho, Y.S., Yoon, S.B. & Seo, S.N., 1995. *Numerical Simulations of the 1960 Chilean Tsunami Propagation and Inundation at Hilo, Hawaii*, pp. 99–115, Springer Netherlands.
- Lotto, G.C., Dunham, E.M., Jeppson, T.N. & Tobin, H.J., 2017a. The effect of compliant prisms on subduction zone earthquakes and tsunamis, *Earth planet. Sci. Lett.*, **458**, 213–222.
- Lotto, G.C., Nava, G. & Dunham, E.M., 2017b. Should tsunami simulations include a nonzero initial horizontal velocity?, *Earth, Planets Space*, **69**(1), 117.
- Lotto, G.C., Jeppson, T.N. & Dunham, E.M., 2018. Fully coupled simulations of megathrust earthquakes and tsunamis in the Japan Trench, Nankai Trough, and Cascadia Subduction Zone, *Pure appl. Geophys.*, **176**, 4009–4041.
- Lotto, G.C., Jeppson, T.N. & Dunham, E.M., 2019. Fully coupled simulations of megathrust earthquakes and tsunamis in the Japan Trench, Nankai Trough, and Cascadia subduction zone, *Pure appl. Geophys.*, **176**(9), 4009–4041.
- Lozos, J.C. & Harris, R.A., 2020. Dynamic rupture simulations of the m6.4 and m7.1 July 2019 Ridgecrest, California, earthquakes, *Geophys. Res. Lett.*, **47**(7), e2019GL086020.
- Ma, S., 2012. A self-consistent mechanism for slow dynamic deformation and large tsunami generation for earthquakes in the shallow subduction zone, *Geophys. Res. Lett.*, **39**(11), 1–7.
- Ma, S. & Nie, S., 2019. Dynamic wedge failure and along-arc variations of tsunami genesis in the Japan trench margin, *Geophys. Res. Lett.*, **46**(15), 8782–8790.
- Maeda, T. & Furumura, T., 2011. FDM Simulation of seismic waves, ocean acoustic waves, and tsunamis based on tsunami-coupled equations of motion, *Pure appl. Geophys.*, **170**(1–2), 109–127.
- Maeda, T., Furumura, T., Sakai, S. & Shinohara, M., 2011. Significant tsunami observed at ocean-bottom pressure gauges during the 2011 off the Pacific coast of Tohoku Earthquake, *Earth, Planets Space*, **63**(7), 803–808.
- Maeda, T., Furumura, T., Noguchi, S., Takemura, S., Sakai, S., Shinohara, M., Iwai, K. & Lee, S.J., 2013. Seismic- and Tsunami-wave propagation of the 2011 off the Pacific Coast of Tohoku earthquake as inferred from the Tsunami-coupled finite-difference simulation, *Bull. seism. Soc. Am.*, **103**(2B), 1456–1472.
- Maeda, T., Obara, K., Shinohara, M., Kanazawa, T. & Uehira, K., 2015. Successive estimation of a tsunami wavefield without earthquake source data: a data assimilation approach toward real-time tsunami forecasting, *Geophys. Res. Lett.*, **42**(19), 7923–7932.
- Mai, P.M. & Thingbaijam, K.K., 2014. SRCMOD: an online database of finite-fault rupture models, *Seismol. Res. Lett.*, **85**(6), 1348–1357.
- Mai, P.M. *et al.*, 2016. The earthquake-source inversion validation (SIV) project, *Seismol. Res. Lett.*, **87**(3), 690–708.
- Mandli, K.T. *et al.*, 2016. Clawpack: building an open source ecosystem for solving hyperbolic PDES, *PeerJ Comp. Sci.*, **2**, e68.
- McCloskey, J. *et al.*, 2008. Tsunami threat in the Indian Ocean from a future megathrust earthquake west of Sumatra, *Earth planet. Sci. Lett.*, **265**(1–2), 61–81.
- Meister, O., Rahnema, K. & Bader, M., 2016. Parallel, memory efficient adaptive mesh refinement on structured triangular meshes with billions of grid cells, *ACM Trans. Math. Softw.*, **43**(3), 19:1–19:27.
- Melgar, D., Williamson, A.L. & Salazar-Monroy, E.F., 2019. Differences between heterogenous and homogenous slip in regional tsunami hazards modelling, *J. geophys. Int.*, **219**(1), 553–562.
- Murotani, S., Iwai, M., Satake, K., Shevchenko, G. & Loskutov, A., 2015. Tsunami Forerunner of the 2011 Tohoku Earthquake Observed in the Sea of Japan, *Pure appl. Geophys.*, **172**(3–4), 683–697.
- Murphy, S. *et al.*, 2016. Shallow slip amplification and enhanced tsunami hazard unravelled by dynamic simulations of mega-thrust earthquakes, *Sci. Rep.*, **6**, 35007.
- Murphy, S. *et al.*, 2018. Tsunamigenic earthquake simulations using experimentally derived friction laws, *Earth planet. Sci. Lett.*, **486**, 155–165.
- Noda, H., 2008. Frictional constitutive law at intermediate slip rates accounting for flash heating and thermally activated slip process, *J. geophys. Res.*, **113**(B9), B09302.
- Oeser, J., Bunge, H.-P. & Mohr, M., 2006. Cluster design in the earth sciences: Tethys, in *International Conference on High Performance Computing and Communications*, pp. 31–40, Springer.
- Oglesby, D.D., Archuleta, R.J. & Nielsen, S.B., 2000. The three-dimensional dynamics of dipping faults, *Bull. seism. Soc. Am.*, **90**(3), 616–628.
- Okada, Y., 1985. Surface deformation due to shear and tensile faults in a half-space, *Bull. seism. Soc. Am.*, **75**(4), 1135–1154.
- Okal, E.A., 1982. Mode-wave equivalence and other asymptotic problems in tsunami theory, *Phys. Earth planet. Inter.*, **30**(1), 1–11.
- Pelties, C., De La Puente, J., Ampuero, J.P., Brietzke, G.B. & Käser, M., 2012. Three-dimensional dynamic rupture simulation with a high-order discontinuous Galerkin method on unstructured tetrahedral meshes, *J. geophys. Res.*, **117**(2), 1–15.
- Pelties, C., Gabriel, A.A. & Ampuero, J.P., 2014. Verification of an ADER-DG method for complex dynamic rupture problems, *Geoscient. Model Dev.*, **7**(3), 847–866.
- Poisson, B., Oliveros, C. & Pedreros, R., 2011. Is there a best source model of the Sumatra 2004 earthquake for simulating the consecutive tsunami?, *J. geophys. Int.*, **185**(3), 1365–1378.
- Preuss, S., Ampuero, J.P., Gerya, T. & van Dinther, Y., 2020. Characteristics of earthquake ruptures and dynamic off-fault deformation on propagating faults, *Solid Earth*, **11**(4), 1333–1360.
- Pritchard, M.E., Norabuena, E.O., Ji, C., Boroschek, R., Comte, D., Simons, M., Dixon, T.H. & Rosen, P.A., 2007. Geodetic, teleseismic, and strong motion constraints on slip from recent southern Peru subduction zone earthquakes, *J. geophys. Res.*, **112**(B3), B03307.
- Ramos, M.D. & Huang, Y., 2019. How the transition region along the Cascadia megathrust influences coseismic behavior: insights from 2-D dynamic rupture simulations, *Geophys. Res. Lett.*, **46**(4), 1973–1983.
- Rettenberger, S., 2017. PUMGen, <https://github.com/SeisSol/PUMGen>.
- Rettenberger, S., Meister, O., Bader, M. & Gabriel, A.-A., 2016. ASAGI: A parallel server for adaptive geoinformation, in *Proceedings of the Exascale Applications and Software Conference 2016 on - EASC '16*, pp. 1–9, ACM Press.
- Roten, D., Olsen, K.B., Day, S.M., Cui, Y. & Fäh, D., 2014. Expected seismic shaking in Los Angeles reduced by San Andreas fault zone plasticity, *Geophys. Res. Lett.*, **41**(8), 2769–2777.
- Ryan, K.J., Geist, E.L., Barall, M. & Oglesby, D.D., 2015. Dynamic models of an earthquake and tsunami offshore Ventura, California, *Geophys. Res. Lett.*, **42**(16), 6599–6606.
- Saito, T., 2017. Tsunami generation: validity and limitations of conventional theories, *J. geophys. Int.*, **210**(3), 1888–1900.
- Saito, T. & Kubota, T., 2019. Tsunami modeling for the deep sea and inside focal areas tsunami modeling including earthquake rupture and seismic

- waves contributes to mega-thrust earthquake investigation and disaster mitigation, *Annu. Rev. Earth Planet. Sci.*, **48**, 121–145.
- Saito, T., Baba, T., Inazu, D., Takemura, S. & Fukuyama, E., 2019. Synthesizing sea surface height change including seismic waves and tsunami using a dynamic rupture scenario of anticipated Nankai trough earthquakes, **769**, doi:10.1016/j.tecto.2019.228166.
- Salaree, A. & Okal, E.A., 2020. Effects of bathymetry complexity on tsunami propagation: a spherical harmonics approach, *J. geophys. Int.*, **223**(1), 632–647.
- Schmeling, H. et al., 2008. A benchmark comparison of spontaneous subduction models—towards a free surface, *Phys. Earth planet. Inter.*, **171**(1–4), 198–223.
- Seno, T., 2014. Stress drop as a criterion to differentiate subduction zones where  $M_w 9$  earthquakes can occur, *Tectonophysics*, **621**, doi:10.1016/j.tecto.2014.02.016.
- Shearer, P. & Burgmann, R., 2010. Lessons learned from the 2004 Sumatra-Andaman megathrust rupture, *Annu. Rev. Earth Planet. Sci.*, **38**, 103–31.
- Shi, F., Kirby, J.T., Harris, J.C., Geiman, J.D. & Grilli, S.T., 2012. A high-order adaptive time-stepping TVD solver for Boussinesq modeling of breaking waves and coastal inundation, *Ocean Modell.*, **43–44**, 36–51.
- Sobolev, S.V. & Muldashev, I.A., 2017. Modeling seismic cycles of great megathrust earthquakes across the scales with focus at postseismic phase, *Geochem. Geophys. Geosyst.*, **18**(12), 4387–4408.
- Song, Y.T., Fu, L.-L., Zlotnicki, V., Ji, C., Hjorleifsdottir, V., Shum, C. & Yi, Y., 2008. The role of horizontal impulses of the faulting continental slope in generating the 26 December 2004 tsunami, *Ocean Modelling*, **20**(4), 362–379.
- Stephenson, W., Reitman, N. & Angster, S., 2017. U.S. Geological Survey Open-File Report 2017–1152: P- and S-wave velocity models incorporating the Cascadia subduction zone for 3D earthquake ground motion simulations, version 1.6—Update for Open-File Report 2007–1348, Tech. rep., U.S. Geological Survey.
- Sun, T., Wang, K., Fujiwara, T., Kodaira, S. & He, J., 2017. Large fault slip peaking at trench in the 2011 Tohoku-oki earthquake, *Nat. Commun.*, **8**, 14044.
- Synolakis, C.E., Bernard, E.N., Titov, V.V., Kânoğlu, U. & González, F.I., 2008. Validation and verification of tsunami numerical models, *Pure appl. Geophys.*, **165**(11–12), 2197–2228.
- Tanioka, Y. & Satake, K., 1996. Tsunami generation by horizontal displacement of ocean bottom, *Geophys. Res. Lett.*, **23**(8), 861–864.
- Titov, V.V. & Gonzalez, F.I., 1997. Implementation and testing of the method of splitting tsunami (MOST) model, NOAA Technical Memorandum ERL PMEL-112, Pacific Marine Environmental Laboratory, Seattle, WA, USA.
- Tong, X. & Lavier, L., 2018. Simulation of slip transients and earthquakes in finite thickness shear zones with a plastic formulation, *Nat. Commun.*, **9**, doi:10.1038/s41467-018-06390-z.
- Ulrich, T., Gabriel, A.-A., Ampuero, J.-P. & Xu, W., 2019a. Dynamic viability of the 2016 Mw 7.8 Kaikōura earthquake cascade on weak crustal faults, *Nat. Commun.*, **10**(1), 1213.
- Ulrich, T. et al., 2019b. Coupled, physics-based modeling reveals earthquake displacements are critical to the 2018 Palu, Sulawesi Tsunami, *Pure appl. Geophys.*, **176**, 4069–4109.
- Ulrich, T., Gabriel, A. & Madden, E.H., 2020. Stress, rigidity and sediment strength control megathrust earthquake and tsunami dynamics, doi:10.31219/osf.io/9kdhb.
- Uphoff, C., Rettenberger, S., Bader, M., Madden, E., Ulrich, T., Wollherr, S. & Gabriel, A.-A., 2017. Extreme scale multi-physics simulations of the tsunamigenic 2004 Sumatra megathrust earthquake, in *Proceedings of the International Conference for High Performance Computing, Networking, Storage and Analysis, SC 2017*.
- USGS, accessed 2019-07-22, United states geological survey, m 8.4 - near the coast of southern peru, [https://earthquake.usgs.gov/earthquakes/eventpage/official20010623203314130\\_33/impact](https://earthquake.usgs.gov/earthquakes/eventpage/official20010623203314130_33/impact).
- USGS, accessed 2020-07-03, United states geological survey, m 8.4 - near the coast of southern sumatra, [https://earthquake.usgs.gov/earthquakes/eventpage/official20070912111026830\\_34/impact](https://earthquake.usgs.gov/earthquakes/eventpage/official20070912111026830_34/impact).
- van Dinther, Y., Gerya, T.V., Dalguer, L.A., Corbi, F., Funiciello, F. & Mai, P.M., 2013a. The seismic cycle at subduction thrusts: 2. Dynamic implications of geodynamic simulations validated with laboratory models, *J. geophys. Res.*, **118**(4), 1502–1525.
- van Dinther, Y., Gerya, T.V., Dalguer, L.A., Mai, P.M., Morra, G. & Giardini, D., 2013b. The seismic cycle at subduction thrusts: insights from seismo-thermo-mechanical models, *J. geophys. Res.*, **118**(12), doi:10.1002/2013JB010380.
- van Dinther, Y., Mai, P.M., Dalguer, L.A. & Gerya, T.V., 2014. Modeling the seismic cycle in subduction zones: the role and spatiotemporal occurrence of off-megathrust events, *Geophys. Res. Lett.*, **41**(4), 1194–1201.
- van Zelst, I., Wollherr, S., Gabriel, A.-A., Madden, E.H. & van Dinther, Y., 2019. Modeling megathrust earthquakes across scales: One-way coupling from geodynamics and seismic cycles to dynamic rupture, *J. geophys. Res.*, **124**(11), 11414–11446.
- Vater, S. & Behrens, J., 2014. Well-balanced inundation modeling for shallow-water flows with Discontinuous Galerkin schemes, in *Finite Volumes for Complex Applications VII – Elliptic, Parabolic and Hyperbolic Problems*, Vol. 78 of Springer Proceedings in Mathematics & Statistics, pp. 965–973, Springer.
- Vater, S., Beisiegel, N. & Behrens, J., 2015. A limiter-based well-balanced discontinuous Galerkin method for shallow-water flows with wetting and drying: one-dimensional case, *Adv. Water Resour.*, **85**, 1–13.
- Vater, S., Beisiegel, N. & Behrens, J., 2017. Comparison of wetting and drying between a RKDG2 method and classical FV based second-order hydrostatic reconstruction, in *Finite Volumes for Complex Applications VIII - Hyperbolic, Elliptic and Parabolic Problems*, pp. 237–245, Springer.
- Vater, S., Beisiegel, N. & Behrens, J., 2019. A limiter-based well-balanced discontinuous Galerkin method for shallow-water flows with wetting and drying: triangular grids, *Int. J. Numer. Methods Fluids*, **91**(8), 395–418.
- Wang, Y., Day, S.M. & Denolle, M.A., 2019. Geometric controls on pulse-like rupture in a dynamic model of the 2015 Gorkha earthquake, *J. geophys. Res.*, **124**(2), 1544–1568.
- Ward, S.N., 1980. Relationships of tsunami generation and an earthquake source, *J. Phys. Earth*, **28**, 441–474.
- Watada, S., Kusumoto, S. & Satake, K., 2014. Traveltime delay and initial phase reversal of distant tsunamis coupled with the self-gravitating elastic Earth, *J. geophys. Res.*, **119**(5), 4287–4310.
- Wendt, J., Oglesby, D.D. & Geist, E.L., 2009. Tsunamis and splay fault dynamics, *Geophys. Res. Lett.*, **36**(15), doi:10.1029/2009GL038295.
- Weng, H. & Yang, H., 2018. Constraining frictional properties on fault by dynamic rupture simulations and near-field observations, *J. geophys. Res.*, **123**(8), 6658–6670.
- Wolf, S., Gabriel, A.-A. & Bader, M., 2020. Optimisation and local time stepping of an ADER-DG scheme for fully anisotropic wave propagation in complex geometries, no title, in *Proceedings of the 10th International Workshop on Advances in High-Performance Computational Earth Sciences: Applications & Frameworks*, Amsterdam, Netherlands, June 3–5, 2020.
- Wollherr, S., Gabriel, A.A. & Uphoff, C., 2018. Off-fault plasticity in three-dimensional dynamic rupture simulations using a modal Discontinuous Galerkin method on unstructured meshes: implementation, verification and application, *J. geophys. Int.*, **214**(3), 1556–1584.
- Wollherr, S., van Zelst, I., Gabriel, A.-A., Madden, E. & van Dinther, Y., 2019. Plastic deformation and seafloor uplift in geomechanically constrained dynamic rupture models of subduction zone earthquakes, in *Proceedings of the EGU General Assembly; Geophysical Research Abstracts*, Vol. 21, EGU2019-14651.

## APPENDIX A: AVAILABILITY OF SOFTWARE AND REPRODUCIBILITY INFORMATION

### A1 Earthquake modelling: SeisSol

The earthquake simulation software SeisSol ([www.seissol.org](http://www.seissol.org)) is publicly available as open source software at <https://github.com/S-eisSol/SeisSol>. Documentation how to compile and use SeisSol is provided at <https://seissol.readthedocs.io/>.

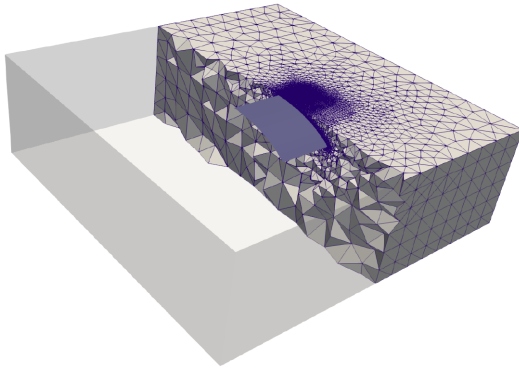


**Figure A1.** Structural model and mesh used for the subduction-initialized dynamic earthquake rupture model in Scenario C (Section 4).

SeisSol has been validated against a series of wave propagation and dynamics rupture benchmarks (see the references provided in Section 2.1) which are described in the ‘‘Cookbook’’ section of <https://seissol.readthedocs.io/>.

## A2 Tsunami modelling: sam(oa)<sup>2</sup>-flash

The sam(oa)<sup>2</sup>-flash tsunami model (Section 2.2) has been implemented within the sam(oa)<sup>2</sup> framework, which is publicly available as open source software at <https://gitlab.lrz.de/samoam/samoam>. Documentation on how to compile and use sam(oa)<sup>2</sup> and sam(oa)<sup>2</sup>-flash is provided at <https://samoam.readthedocs.io/>. The sam(oa)<sup>2</sup>-flash version used in this paper is permanently archived in the gitlab repository, as branch `samoam-flash-gji-2020`.

Sam(oa)<sup>2</sup>-flash has been validated against a set of community benchmarks, following the test suite also used for validation of the underlying discontinuous Galerkin scheme, Stormflash2D (Vater *et al.* 2017). These benchmarks include tests for steady state solutions (Resting Lake) and the inundation of coasts (Oscillating Lake, Okushiri Tsunami). The archive at <https://zenodo.org/record/383668> includes instructions and required data files to reproduce these benchmarks. Results including a comparison to reference solutions are available at [https://zenodo.org/record/3836668/files/documentation\\_overview.pdf](https://zenodo.org/record/3836668/files/documentation_overview.pdf).

Tsunami modelling that includes inundation must handle varying spatial scales. Sam(oa)<sup>2</sup>-flash uses adaptive mesh refinement (e.g. LeVeque *et al.* 2011), currently the most advanced approach for tsunami model meshing. This is in contrast to traditional tsunami modelling approaches using a multitude of nested grids (e.g. Liu *et al.* 1995; Titov & Gonzalez 1997) or the alternative approach consisting of non-uniform, predefined meshes that use *a priori* knowledge about the wave behaviour to assign high-resolution areas (Harig *et al.* 2008).

## A3 Reproducibility

We provide all necessary information and data sets required to reproduce the results presented in this work at <https://tinyurl.com/yxn6zrqc>. The archive includes all required configuration files, compilation parameters and input data.

## APPENDIX B: MESH GENERATION FOR DYNAMIC RUPTURE MODELLING WITH SeisSol

The structural model and mesh for the earthquake physical model used in scenarios A and B are generated with the open-source software Gmsh ([www.gmsh.info](http://www.gmsh.info)) (Geuzaine & Remacle 2009). The structural model in Scenario C is built in GOCAD ([www.pdgm.com](http://www.pdgm.com)) and automatized mesh generation is performed with the software PUMGen (<https://github.com/SeisSol/PUMGen/>, Rettenberger 2017), which also exports the mesh into the efficient PUML format used by SeisSol. PUMGen embeds MeshSim from SimMetrix, the underlying mesh generator of SimModeler ([www.simmatrix.com](http://www.simmatrix.com)), such that the mesh generation may be run in parallel on a compute cluster. The scenarios presented here use mesh sizes of 13 million elements (Scenario C) and 16 million elements (scenarios A and B), which require computational resources well within the scope of typical applications for supercomputing centres or university clusters.

Spatial resolution of earthquake faults has to be small enough to adequately resolve the dynamics behind the earthquake rupture front, where shear stress and slip rate vary significantly. The so-called cohesive zone, by analogy to tensile fracture mechanics, captures shear stress breaking down from its static to its dynamic value (Day *et al.* 2005). In the dynamic earthquake models used in scenarios A and B (Section 3.1), 400 m element edge lengths on the fault are combined with polynomial degree  $p = 5$  (spatio-temporal order of accuracy of 6) leading to an effective numerical discretization distinctively higher. SeisSol’s underlying numerical scheme defines initial conditions such as shear and normal stress at two-dimensional quadrature points located inside each tetrahedral element face which is linked to the fault (Pelties *et al.* 2014). The effective resolution of the fault can be approximated by the edge length of the mesh divided by  $p + 2$  additional integration points (De La Puente *et al.* 2009). This sets on-fault resolution to  $400/7 = 57$  m which properly resolves the minimum cohesive zone width of 150 m and creates a 16 million element mesh. The nucleation patch has a reduced mesh element edge length of 250 m. Failure initiates and evolves into a sustained rupture as the friction is decreased over time in this region. Following Wollherr *et al.* (2018), assessing the worst local resolution achieved, we determine the following expected maximum errors for the results with this mesh: 0.09 per cent for the rupture arrival, 7.6 per cent for the peak slip rate, and 0.8 per cent for the final slip magnitude. These meet the recommendations from Day *et al.* (2005) for acceptable errors.

For the subduction-initialized dynamic earthquake model in Scenario C (Section 4.1.1), we discretize the structural model with an element edge length of 1 km on the fault, 5 km within a mesh refinement zone surrounding the fault, and a maximum element edge length of 20 km. This properly resolves a minimum cohesive zone width of 193 m, which is appropriate along most of the fault. In Scenario C, it also is crucial that the meshed 3-D fault matches the locations of the 2D fault from the subduction slip event (see Section D). We achieve this by extruding the 2-D fault from the subduction model along strike in GOCAD ([www.pdgm.com](http://www.pdgm.com)), with straight horizontal lines between points at the same depth and no smoothing.

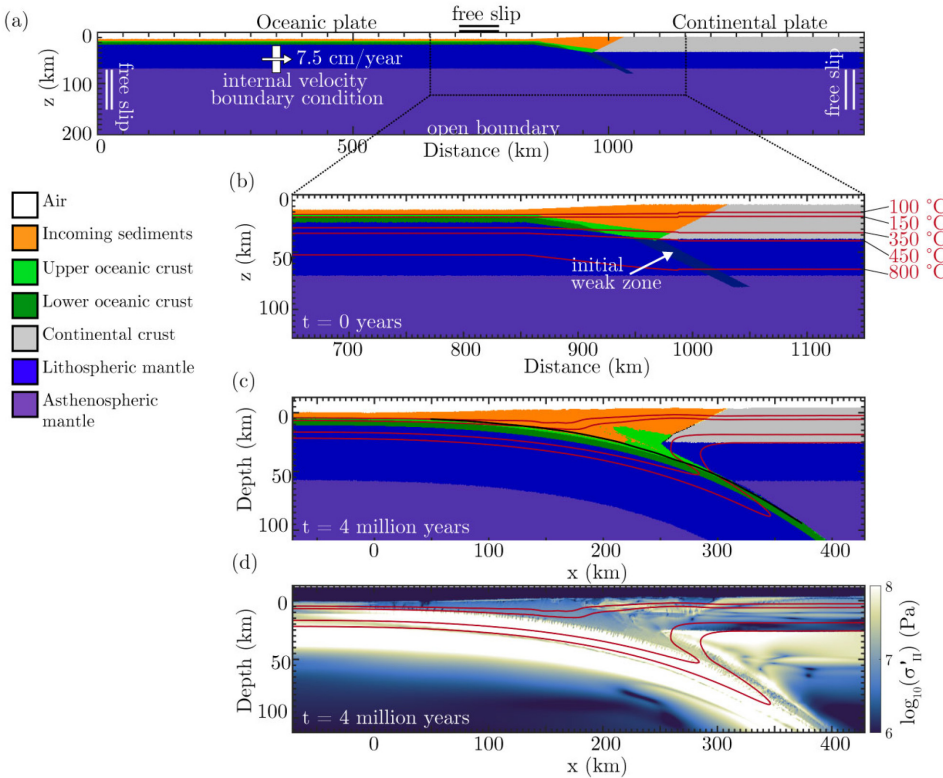


**Figure A2.** (a, b) Set-up of the subduction physical model and (c) final geometry of the subduction zone at the approximate time of the slip event used to initialize the earthquake model in Scenario C (Section 4). (d) Log of the second invariant of the deviatoric stress tensor,  $\sigma'_{II}$ , which controls yielding in the subduction model (see eq. C1). Note that the coordinates change from (a, b) to (c, d) to coincide with the developed trench.

**Table A1.** Reference material properties of the subduction model.

Material	$\rho$ (kg m <sup>-3</sup> )	$G$ (GPa)	$\mu_s^{sc}$ (–)	$\mu_d^{sc}$ (–)	$C$ (MPa)
Sediments	2600	5	0.35	0.105	2.5
Continental crust	2700	12	0.72	0.216	10
Upper oceanic crust	3000	12	0.5	0.15	5
Lower oceanic crust	3000	12	0.85	0.255	15
Mantle	3300	35	0.6	0.18	20

## APPENDIX C: GEODYNAMIC SEISMIC CYCLE MODEL

The physical subduction model that we use has an extent of 1500 km in the  $x$ -direction by 200 km in the  $z$ -direction. The subducting oceanic plate consists of 4 km thick sediments, a 2 km thick basaltic upper crust, a 5 km thick gabbroic lower oceanic crust, and a lithospheric mantle (Fig. A2a; Table A1). The continental plate consists of a sedimentary wedge, an upper and lower continental crust and a lithospheric mantle layer. A constant velocity of 7.5 cm yr<sup>-1</sup> is applied to a small box inside the subducting plate to initiate and sustain subduction. At the sides and the top of the model, free slip boundary conditions are applied that only allow for tangential velocities along the boundary, while perpendicular velocities are not permitted. There is an open boundary at the bottom of the model where material can flow out, while free slip is externally applied (Gorczyk *et al.* 2007). The sticky air approximation, common in geodynamic modelling where topography develops, mimics an internal free surface, as low density, low viscosity ‘sticky air’ material is decoupled from the underlying rocks (Schmeling *et al.* 2008; Crameri *et al.* 2012).

The subduction geometry, lithological properties, temperature, viscosity, stresses and strengths develop spontaneously over 3.6 million years through solving thermomechanical conservation equations with a time step of 1000 yr (compare Figs A2b and c). At temperatures below 100 °C, materials are velocity strengthening and a transition between 100 and 150 °C leads to velocity weakening at higher temperatures. The downdip limit of the seismogenic zone develops as viscous deformation becomes progressively more dominant at temperatures above 350 °C (van Dinther *et al.* 2013b).

After 3.6 Myr, a sufficiently steady-state subduction geometry has developed, suitable for a seismic cycle. The time step is gradually reduced by manually predefined intervals to 5 yr, after which the seismic cycle phase of the model begins and lasts for approximately 30 000 yr. The subduction geometry (Fig. A2c) shows the oceanic plate subducting with an average dip of 14.8° above 95 km depth during this phase.

After a spin-up period at the start of the seismic cycle phase, tens of quasi-periodic slip events occur [see van Zelst *et al.* (2019), fig 3]. We refer to these as ‘slip events’ to differentiate them from earthquakes modelled with SeisSol. These slip events represent sudden, spontaneous increases of plastic strain rates during localized plastic failure in a narrow shear band (the ‘fault’ in the subduction model), which leads to reversed velocities due to elastic rebound and a drop of elastic stresses that were built up by the convergence of the subducting plate towards the overriding plate. Brittle failure is simulated according to Drucker-Prager plasticity and initiates when the second invariant of the deviatoric stress tensor  $\sigma'_{II}$  (Fig. A2d) meets the yield strength:

$$\sigma'_{II} = C + \mu^{sc} \left[ 1 - (P_f/P) \right] P. \quad (C1)$$

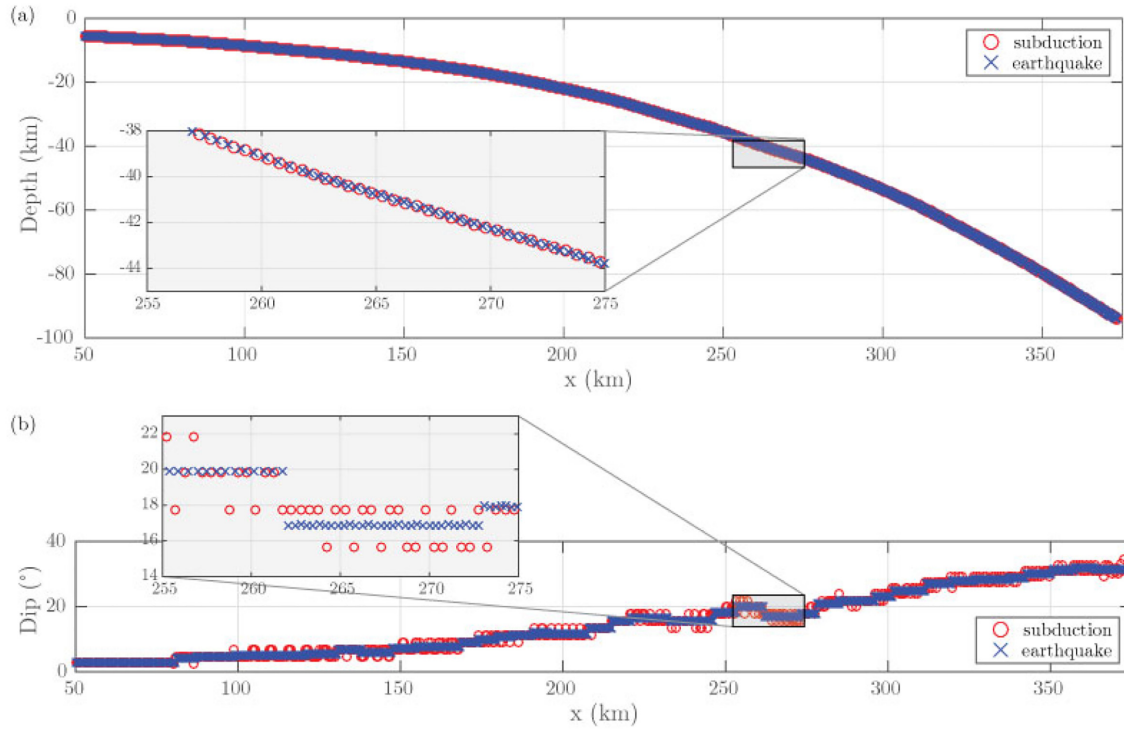


**Figure A3.** Comparison between (a) locations and (b) dip of faults in the subduction and earthquake models in Scenario C.

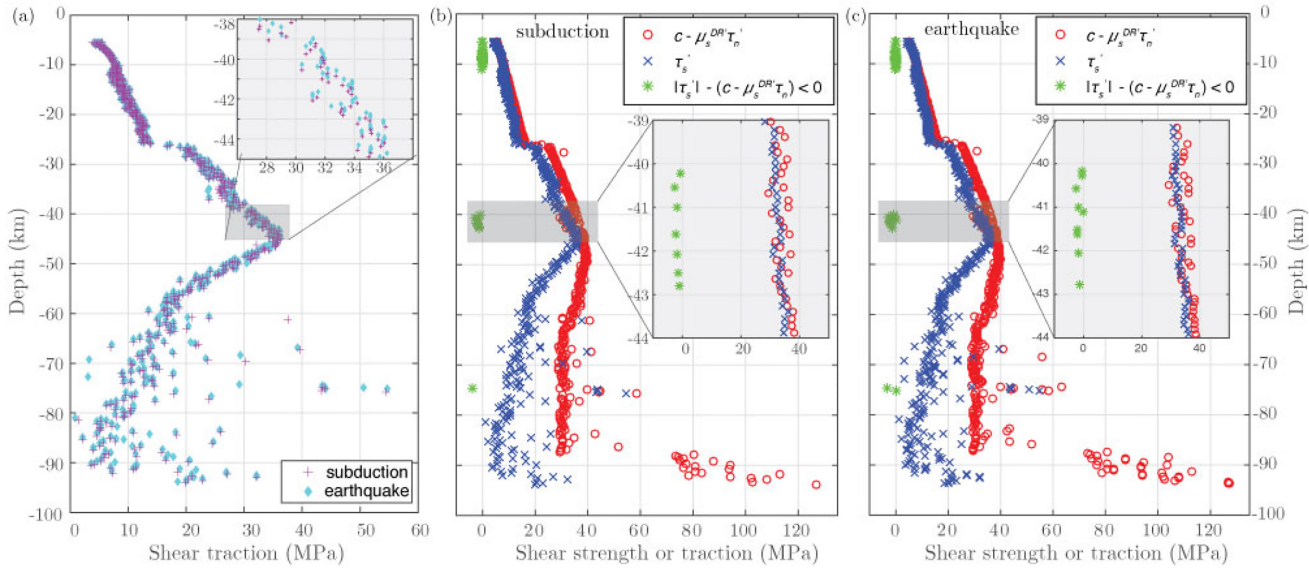


**Figure A4.** (a) Comparison between the effective shear traction,  $\tau'_s$ , on the faults in the subduction and earthquake models in Scenario C before changes are made to  $c$  in the sediments and to  $\mu_s$  at outliers, as discussed in the text. Failure analysis according to the earthquake model failure criterion (eq. 3) at points (b) along the subduction model fault and (c) along a slice at  $y = 0$  through the earthquake model fault. Variables are defined in text near eq. (3).

Here,  $C$  is cohesion,  $P$  is the mean pressure,  $P_f$  is the pore fluid pressure and  $\mu$  is the friction coefficient. Note that in the subduction model, there is no differentiation between bulk cohesion of intact rock and on-fault cohesion,  $c$ , after failure. We define the onset of a slip event as the first time step at which two adjacent points are at plastic failure (van Zelst *et al.* 2019). At this stage maximum slip rates are around  $5.5 \times 10^{-11} \text{ m s}^{-1}$ , with maximum slip rates of  $9.3 \times 10^{-9} \text{ m s}^{-1}$  reached during the entire event. We know that this localized failure develops into a slip event because we select it from

the series of events after running the entire seismic cycling phase of the subduction model (see Section 5.2 for further discussion).

Slip behaviour after failure is viscoplastic rate dependent. In the strongly slip rate-dependent friction formulation (van Dinther *et al.* 2013a), the friction coefficient  $\mu^{\text{sc}}$  drops non-linearly from the static coefficient  $\mu_s^{\text{sc}}$  to the dynamic coefficient  $\mu_d^{\text{sc}}$  with increasing slip rate  $V$ , according to:

$$\mu^{\text{sc}} = \frac{V_c \mu_s^{\text{sc}} + V \mu_d^{\text{sc}}}{V_c + V}, \quad (\text{C2})$$

where  $V_c$  is the characteristic velocity at which half of the friction drop occurs.

Slip events occur mainly in the model subduction channel and the accretionary wedge. The events typically nucleate near the downdip limit of the model seismogenic zone in the basalt, after which they progress into the shallow sediments.

We choose one representative slip event to initialize the earthquake model. This event is chosen late in the simulation time of the seismic cycling, to ensure that the change of time step has no lasting effect on the slip events. In the chosen slip event, slip initiates at  $x = 220$  km (according to the axis in Figs A2c and d) and proceeds mainly updip, where it is stalled in the velocity strengthening region. Slip also arrests downdip, in the domain dominated by ductile creep.

#### APPENDIX D: ASSESSMENT OF ACCURACY IN MAPPING THE SLIP EVENT CONDITIONS TO THE EARTHQUAKE MODEL

To accurately map subduction model parameters to the earthquake model, it is crucial that the faults in both models are of the same geometrical shape. This ensures that they experience the same stress field and host the same on-fault properties. To verify this, before running the earthquake model, we compare fault locations, fault dip, effective shear traction, and failure on the 2-D subduction model fault and along a 2-D slice at  $y = 0$  through the earthquake model mesh. In the following, we show that the two faults have the same shape and capture the same initial conditions.

Linked parameters of the subduction model fault are available at 649 locations and the slice through the earthquake model fault allows initializing 849 fault locations. Values are ported to the earthquake model at the 500 m resolution of the subduction model. Fig. A3(a) shows that the differences between fault locations are below the 500 m resolution of the subduction model output. Fig. A3(b) shows that the profile of the earthquake model fault is slightly smoother, without the very small variations in dip that are present along the subduction model fault. Along the subduction model fault, the average dip is  $14.8^\circ$ , the minimum dip is  $2.3^\circ$ , and the maximum dip is  $34.4^\circ$ . Along the slice through the earthquake model fault, the average dip is  $14.9^\circ$ , the minimum dip is  $2.8^\circ$ , and the maximum dip is  $31.8^\circ$ .

Variation in shear traction along both faults with depth is shown in Fig. A4. The two model fault host shear tractions that are free of any systematic differences. Along the subduction model fault, the average shear traction magnitude is 14.9 MPa, the minimum is 1.3 MPa, and the maximum is 54.5 MPa. Along the slice through the earthquake model fault, the average shear traction magnitude is 15.0 MPa, the minimum is 0.9 MPa and the maximum is 54.7 MPa.

Fig. A4 shows at each depth the shear traction, the static fault strength, and any points at failure, where the absolute magnitude of the shear traction exceeds the fault strength. Both faults have the same regions at failure: within the sediments and near 42 km depth, where the subduction slip event begins and where we set the nucleation zone in the earthquake model. A zoom into this region reveals that it extends for  $\approx 3$  km with depth along both faults. Note that the slice through the earthquake model fault has more points at failure here, because it has more fault locations overall.